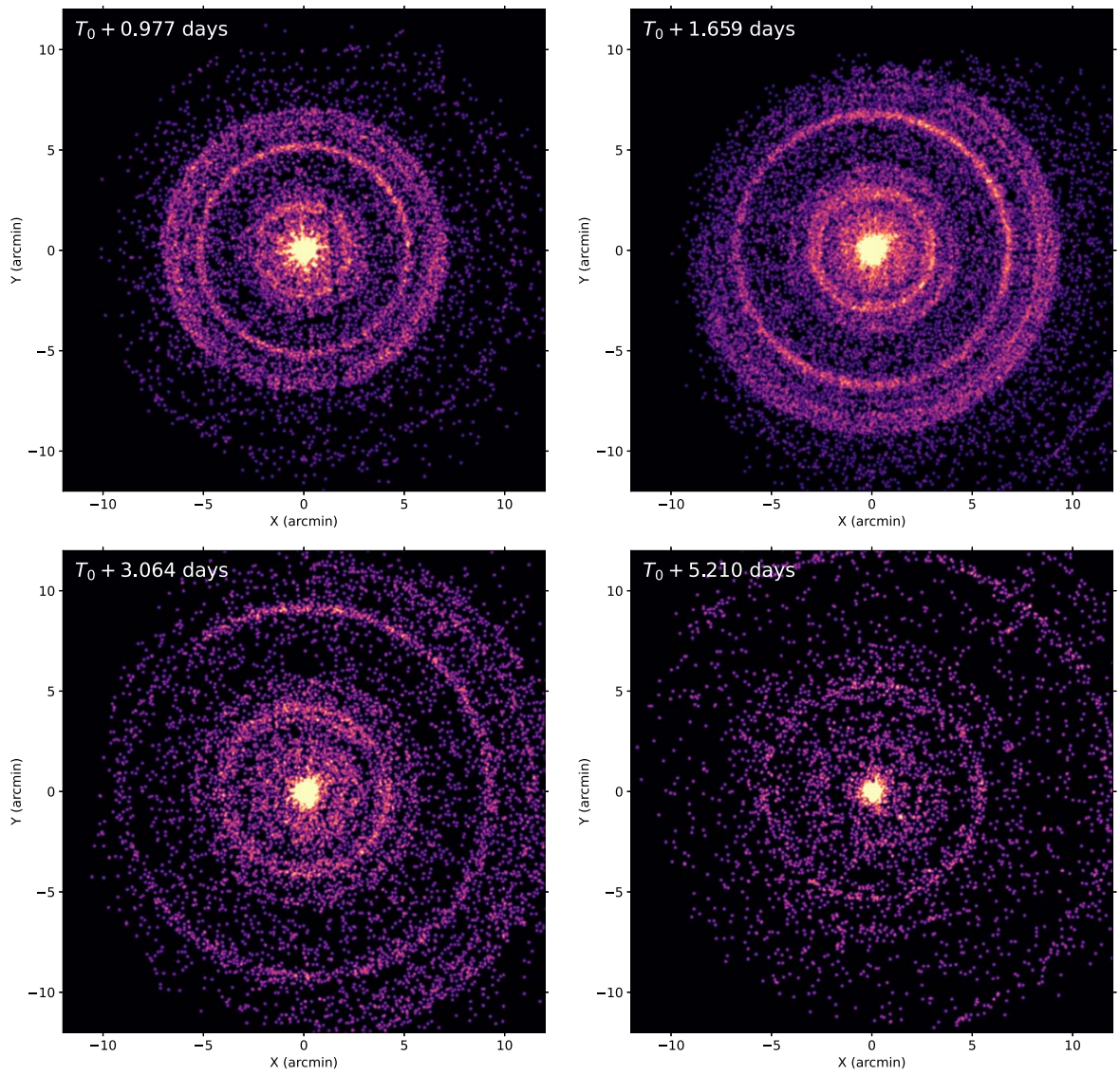

Figure 3. XRT PC-mode 0.8–5.0 keV images from ObsIDs 01126853004 (top left), 01126853006 (top right), 01126853008/09 (bottom left), and 01126853010/11 (bottom right), illustrating the echo expansion with time. The echo event radial positions were scaled by $t^{-0.5}$ to each observation midtime (given in the upper left corner of each image in days since GBM trigger) to counter the halo expansion within each observation.

the PC-mode background region (described in the Appendix B); due to the unusual brightness of the source, we also increased the number of counts per bin by a factor of 10 compared to the default (see Evans et al. 2007 for details). We fit the time-averaged PC-mode spectrum using XSPEC with a power-law model and two absorption components. The first of these was a TBABS fixed to the Galactic value of 5.38×10^{21} cm^{-2} (Willingale et al. 2013); the second was a ZTBABS with $N_{\rm H}$ free and redshift fixed at 0.151.[39] The fit yields $N_{\rm H} = (1.4 \pm 0.4) \times 10^{22}$ cm^{-2}, with a photon index $\Gamma = 1.8 \pm 0.2$. We used these results to convert the light curve into observed 0.3–10 keV flux. The resulting flux measurements are shown in Figure 2.

To investigate possible spectral evolution, we extracted a series of time-resolved spectra using the "Add time-sliced spectrum" option on the UKSSDC website[40] (Evans et al. 2009), which ensures that the modifications to the default processing parameters, described above, are employed. From the WT-mode data, we created one spectrum from the first spacecraft orbit (T_0 + 3.4–4.5 ks), and then spectra in 10 ks chunks from T_0 + 10–50 ks. For PC mode, we extracted spectra over the intervals T_0 + 67–200, 200–400, 400–1000, and >1000 ks. For WT mode, we used only grade 0 events, as is recommended for very absorbed objects.[41] We fitted these spectra independently with the model defined above; the results are shown in Table 1.

[39] We note that there is significant degeneracy between an increased Galactic column density and extinction and/or absorption in the GRB host galaxy. While here and in Section 3.2 we model this effect as due to dust and/or gas in the GRB host, we cannot distinguish between these two scenarios (e.g., Laskar et al. 2023).

[40] https://www.swift.ac.uk/xrt_spectra/01126853/

[41] https://www.swift.ac.uk/analysis/xrt/digest_cal.php#abs

Table 1
Spectral Parameters Determined from Fitting a Power-law Model to the Time-resolved X-Ray Data from Swift, MAXI, and NICER

$T - T_0$ (ks)	Exposure (ks)	Intrinsic N_H (10^{22} cm^{-2})	Photon Index	Fit Stat./d.o.f.	Observatory/Detector
2.5	0.047	⋯	1.75 ± 0.09	307/322	MAXI/GSC
3.4–4.5	1.2	1.28 ± 0.04	1.61 ± 0.02	1249/959	XRT/WT
8.0	0.047	⋯	$2.07^{+0.28}_{-0.26}$	145/166	MAXI/GSC
10.0–20.0	0.5	1.39 ± 0.09	1.89 ± 0.05	859/840	XRT/WT
14.0	0.029	⋯	1.89 ± 0.16	26.9/35	NICER/XTI
19.5	0.062	⋯	1.84 ± 0.15	23.6/36	NICER/XTI
20.0–30.0	2.9	1.36 ± 0.05	$1.84^{+0.02}_{-0.04}$	995/922	XRT/WT
30.0–40.0	1.7	1.25 ± 0.07	1.85 ± 0.04	800/840	XRT/WT
40.0–50.0	2.8	1.20 ± 0.06	1.84 ± 0.03	875/873	XRT/WT
52.6–98.0	2.1	⋯	1.85 ± 0.07	131/153	NICER/XTI
68–175	17	$1.27^{+0.16}_{-0.15}$	1.65 ± 0.08	655/727	XRT/PC
103.0–198.0	6.5	⋯	$1.79 \pm + 0.06$	144/168	NICER/XTI
203.3–360.5	9.8	⋯	$1.61^{+0.10}_{-0.09}$	94/94	NICER/XTI
216–394	12	$1.26^{+0.18}_{-0.17}$	1.80 ± 0.10	632/665	XRT/PC
404–954	26	1.20 ± 0.18	1.92 ± 0.10	501/622	XRT/PC
505.0–961.6	2.7	⋯	1.82 ± 0.19	58.1/67	NICER/XTI
1005–6285	0.24	1.00 ± 0.15	1.91 ± 0.09	723/668	XRT/PC

Note. NICER/XTI and MAXI/GSC data are fit in the energy ranges 4–10 and 4–20 keV, respectively, to avoid contamination from unresolved dust echo contamination, with intrinsic N_H fixed to 1.29×10^{22} cm^{-2}. XRT spectra are fit in the range 0.3–10 keV, allowing for measurement of intrinsic N_H. Note that fit statistics are C-stat (Cash 1979) for MAXI and Swift data; NICER are χ^2. Galactic N_H is fixed to a value of 5.38×10^{21} cm^{-2} (Willingale et al. 2013).

The photon index ranges between ∼1.6 and ∼1.9 with the harder profiles observed during the first block of observations (from 3.4 to 4.5 ks) and around 1–2 days (from 68 to 175 ks) after T_0.

2.3. Swift Ultraviolet/Optical Telescope

The UVOT began settled observations of the field of GRB 221009A at 2022 October 9 14:13:17 UT, $T_0 + 3.4$ ks (179 s after the first BAT trigger; Dichiara et al. 2022; Kuin et al. 2022). A nearby star, 5″ away from the GRB, contaminates the photometry when using the standard circular aperture of 5″ radius. In order to minimize the star's contribution to the measurement of the afterglow, we use a 2.″5 aperture to extract source counts. To be consistent with the UVOT calibration, these count rates were then corrected to 5″ using the curve of growth contained in the calibration files. Background counts were extracted using two circular regions of radius 15″ located in source-free regions identified from stacked deep images in each filter. The count rates were obtained from the image lists using the Swift tool `uvotsource`.

As GRB 221009A fades, even using a small aperture, the contribution from the nearby star increases in dominance. In order to estimate the level of contamination, for each filter, we combined the late-time exposures between $T_0 + (3.4 \times 10^6)$ s and $T_0 + (4.4 \times 10^6)$ s. We extracted the count rate in the late combined exposures using the same 2.″5 aperture and applied an aperture correction to 5″. These were subtracted from the source count rates to obtain the afterglow count rates. The afterglow count rates were converted to magnitudes using the UVOT photometric zero-points (Poole et al. 2008; Breeveld et al. 2011), as well as to fluxes. To improve the signal-to-noise ratio (S/N), the count rates in each filter were binned using $\Delta t/t = 0.2$. The final photometry is plotted in the bottom panel of Figure 2 and listed in Appendix C. We caution that the photometry in the *uvw1* and *uvw2* is likely impacted by red leak; see Siegel et al. (2014), Brown et al. (2010) for additional details.

2.4. MAXI

MAXI, which is on board the International Space Station (ISS), performs scanning observations of about 80% of the sky every 92 minutes. Prior to the GBM detection of the prompt emission from GRB 221009A, the two gas slit camera (GSC; Mihara et al. 2011) units, GSC_4 and GSC_5, scanned the source region at 12:25 UT on 2022 October 9 (T_0−3.1 ks), and no enhancement was seen at that time. The 2–10 keV 3σ upper limit is 0.074 ct cm^{-2} s^{-1}, corresponding to a flux of approximately 7.9×10^{-10} erg cm^{-2} s^{-1}. At 13:58 UT (T_0+2.5 ks) the GSCs detected a very bright transient with a 2–10 keV flux of 5.97 ± 0.19 ct cm^{-2} s^{-1} (∼6.5×10^{-8} erg cm^{-2} s^{-1}; Negoro et al. 2022). Unfortunately, at the time the data were collected, there was a loss of the signal to the ground, and the data were stored in the High Rate Communication Outage Recorder in the ISS, leading to a delay in reporting the transient. Before downloading these stored data at around 15:55 UT, the MAXI/GSC Nova-Alert System (Negoro et al. 2016) triggered on the source at 15:31:03 UT (T_0+8.0 ks), about 81 minutes after the BAT trigger. In this second observation by MAXI, the 2–10 keV flux had dropped to 1.00 ± 0.08 ct cm^{-2} s^{-1} (about 1×10^{-8} erg cm^{-2} s^{-1}).

Thanks to the exceptional brightness, the GSCs significantly detected the afterglow during four scans that followed the second detection, to 21:41 UT, six scans in total (e.g., Kobayashi et al. 2022). Typically, GRBs are not detected beyond the first one or two scans, taken at ∼92 minute intervals. After the six detections, the sky region containing the source was not observable by MAXI until 15:31 UT on 2022 October 11.

We performed a spectral analysis using data obtained from GSC_4 and GSC_5 (for details see Appendix D). We first attempted a standard analysis using the same model applied to

the XRT spectra, i.e., a power law with two absorption components, with a fixed Galactic absorption column density of $N_{\rm H} = 5.38 \times 10^{21}$ cm^{-2}. However, we obtained steeper photon indices and/or lower intrinsic absorption column densities than those of the XRT (see Table 7). If we fixed $N_{\rm H,zabs}$ at the weighted mean value obtained with the XRT at $T_0 + (3.4 - 50)$ ks, 1.29×10^{22} cm^{-2}, even steeper photon indices were obtained.

These discrepancies can be explained by the GSC spectra containing dust scattered soft X-rays, which cannot be spatially resolved by the GSC. Mitigation of the dust scattering process is discussed in Appendix D; to summarize, an additional spectral component to account for the scattered emission was included with a power-law index derived from XRT PC-mode data and the associated flux allowed to vary as a free parameter. The afterglow photon index was fit as a free parameter in the data from the first two scans, but fixed at the weighted mean XRT value at $T_0 + (10 - 50)$ ks due to poor statistics. The resulting spectral parameters are displayed in Table 1, and the flux measurements (extrapolated to the 0.3–10.0 keV band) are plotted in Figure 2.

2.5. NICER

NICER received notification of this GRB from MAXI on the ISS via On-orbit Hookup of MAXI and NICER at 14:10:57 UT, but could not begin regular observations due to poor visibility until $T_0 + 52.870$ ks. Only two observations were possible during this early phase. The first and second observations were at $T_0 + 14.003$ ks and $T_0 + 19.560$ ks with an exposure time of 29 and 62 s, respectively. After $T_0 + 52.870$ ks, NICER intermittently made observations over a period of about 42 days.

NICER's X-ray Timing Instrument (XTI) consists of 56 modules, each comprising an X-ray concentrator optic and silicon drift detector (Gendreau et al. 2012). During these observations, 52 XTI modules were operational. We reduced the data with the `nicerl2` command and generated level (2) cleaned events. To avoid potential contamination of instrumental noise, we further excluded XTI module numbers (14) and (34). We defined a time interval in which an exposure time of more than 200 s can be continuously secured as a one-time interval and created an energy spectrum at each time interval (except for the first two observations) with good statistics.

To select a time period with less background influence due to charged particles, we also checked the distribution of the rate of 12–15 keV photons, where the optics have less effective area. Most data are distributed around 0.048 ct s^{-1} and can be represented by a normal distribution with a standard deviation of 0.018 ct s^{-1}. Therefore, we removed data with a rate greater than 2σ from the mean in the 12–15 keV range after $T_0 +$ 100 ks seconds where the background contribution becomes large (>0.084 ct s^{-1}). We also did not use data after $T_0 +$ 1000 ks because the background rate increased due to a geomagnetic storm. The background spectral model is estimated by the 3C 50 background model (Remillard et al. 2022) using the `nibackgen3c50` command.

To explore the spectral evolution as in Section 2.2, we divided the NICER data into six time intervals and fitted the time-resolved spectra with a power-law model and the same two absorption components. Since NICER is a nonimaging detector, it cannot remove photons originating from the dust echo within its 5′ diameter field of view. To evaluate the impact of the dust echo, we fitted the data in two energy ranges, 1–8 and 4–8 keV bands. Since the data fitting in the 4–8 keV range does not allow us to constrain the intrinsic $N_{\rm H}$ value, we fixed it to 1.29×10^{22} cm^{-2}, which is the weighted mean value obtained by XRT at $T_0 +$ (10.0–961.6) ks (Table 1). Comparing the fitting results in the two energy bands, the results for the 4–8 keV band show that the photon indices are systematically harder than those for the 1–8 keV band results and consistent with the XRT results. Therefore, we conclude that 4–8 keV light curve is much less affected by the dust echo, and report these results in Table 1.

3. Analysis

3.1. Dust Scattering Echo

While complicating the point-source analysis of the afterglow emission, the dust scattering echo contains a rich amount of information about the intervening Galactic dust along the line of sight to GRB 221009A. Dust echoes from GRBs offer the unique opportunity to measure distances to dust clouds geometrically, with a precision limited only by the angular resolution of the telescope. This is because the distance $D_{\rm GRB}$ to the X-ray source is effectively infinite, relative to the distance to the dust. This allows us to eliminate the source distance from the scattering angle equation (e.g., Heinz et al. 2015) and solve it directly for the distance $D_{\rm dust}$ to the dust (using the small angle approximation):

$$D_{\rm dust} = \frac{D_{\rm GRB}}{1 + \frac{D_{\rm GRB}\theta^2}{2c\Delta t}} \approx \frac{2c\Delta t}{\theta^2} \quad (1)$$

where Δt is the time delay between the GRB and the exposure, and θ is the off-axis angle of the ring relative to the position of the GRB.

Because the vast majority of the fluence of the GRB was concentrated in the prompt GRB emission, to the lowest order, we can approximate the input light curve that caused the echo as a delta function in time. This implies that there is a single, unique Δt for each photon detected by the XRT, and thus, each photon can be referenced to a specific dust distance in Equation (1). This makes the analysis of this echo substantially simpler than in comparable echoes from Galactic X-ray transients.

Details of our analysis of the dust echoes from GRB 221009A are provided in Appendix E. Figure 4 shows the best-fit column density histogram for a standard Mathis–Rumpl–Nordsieck (MRN) model (Mathis et al. 1977), assuming a soft X-ray fluence of $\mathcal{F}_{0.8-5\,\rm keV} = 2.1 \times 10^{-3}$ erg cm^{-2} (S. Lesage et al. 2023, in preparation). The figure shows clear evidence for several dust components on the near side of the Galaxy, with the largest column densities found within distances of about 1 kpc, as expected given the Galactic latitude of GRB 221009A.

However, there is also clear evidence for dust at larger distances, located well above the Galactic disk (see also Negro et al. 2023). While the column densities of these dust concentrations are small, the large cross section at the correspondingly small scattering angles of this more distant dust makes the scattering from these clouds detectable in the radial intensity profiles, as can be seen in Figure 13, for example. As such, the dust echo from GRB 221009A proves that echo tomography is exquisitely sensitive to small dust

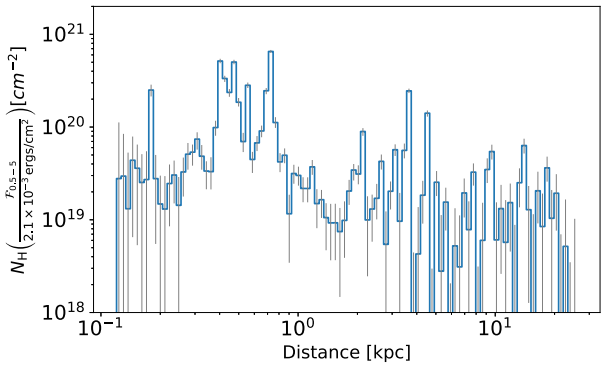

Figure 4. Dust column density (expressed as equivalent hydrogen column density, assuming solar abundances) determined from fitting dust scattering models to the radial intensity profiles as a function of distance, for a standard MRN model. The dependence on the uncertain soft X-ray fluence of GRB 221009A is shown in the *y*-axis label. Vertical gray lines indicate 1σ error bars.

concentrations at large distances that are not typically measurable with other techniques.

The largest column density cloud is located approximately between 400 and 600 pc distance, with a very nearby dust cloud at a distance of about 200 pc and a third cloud at distance approximately 700 pc. Naturally, these structure are very local compared to the large scale Galactic structure. The very rapid detection of the echo by the XRT allows us to map very nearby dust typically hard to study using dust echoes.

We find a total Galactic column density of $N_{\rm H} \sim 5.9 \times 10^{21}$ cm^{-2}, broadly consistent with the Galactic column density of 5.38×10^{21} cm^{-2} found by Willingale et al. (2013). Given that the largest uncertainty in this value derives from the poorly constrained estimate of the soft X-ray fluence of GRB 221009A, we can infer that our assumed fluence of $\mathcal{F}_{0.8-5\,\rm keV} = 2.1 \times 10^{-3}$ erg cm^{-2} is likely correct within roughly 10%.

We find that a simple MRN distribution provides an excellent fit to the temporal evolution of the radial intensity profile, without the need for more complex dust chemistry (such as ice mantles). In this sense, the dust toward GRB 221009A appears to be typical for interstellar dust seen along sightlines to other recent X-ray light echoes, such as the echo from V404 Cyg (Beardmore et al. 2016; Heinz et al. 2016; Vasilopoulos & Petropoulou 2016).

3.2. Broadband Spectral Energy Distribution

The combined XRT+MAXI+NICER data set allows us to explore the soft X-ray afterglow evolution in great detail. In the earliest soft X-ray spectra ($T_0 + 2.5$–10 ks), the afterglow exhibits strong spectral evolution, with the XRT WT-mode power-law photon index increasing (i.e., getting softer) by ∼17% (Table 1). This change is much larger than the inferred WT-mode systematic uncertainty (Appendix B), and is corroborated by the 2–20 keV MAXI spectra derived around this time (Appendix D).

From $T_0 + 10$–50 ks, the spectra show no definitive signs of evolution; there are hints at a reduction in the host galaxy absorption throughout the XRT WT-mode data, although this trend is reversed when XRT switched to PC mode. Given the differences between the WT- and PC-mode results are much less than the dust-induced systematics on the WT results (Appendix B), and no similar spectral evolution is observed in the NICER spectra, we do not believe there is supportable evidence for spectral evolution at these times.

On the longer timescales probed by the XRT PC-mode data, clear spectral evolution is seen and takes the form of an increasing (i.e., softer) photon index, which is confirmed by the 4–8 keV NICER spectra (Table 1).

To constrain the broadband spectral behavior, we built and fit two spectral energy distributions (SEDs) at $T_0 + 4.2$ ks and $T_0 + 43$ ks, following the procedure outlined in Schady et al. (2007, 2010), using data from the BAT survey mode, XRT, and UVOT. For the 4.2 ks SED, we use data in the range 2.5–4.7 ks. For the 43 ks SED, we used data in the range 23–103 ks. Details of the SED construction are provided in Appendix F.

The SEDs were fit using XSPEC. We tested two different models for the continuum: a single power law, and a broken power law with the change in spectral slope fixed to be $\Delta\beta = 0.5$ (corresponding to the expected change in spectral slope caused by the synchrotron cooling frequency; Sari et al. 1998). In each of these models, we also included two dust and gas multiplicative components to account for the Milky Way and host galaxy dust extinction and photoelectric absorption (TBABS, ZTBABS, ZDUST).[42] We also include a component for attenuation by the intergalactic medium (ZIGM). The Galactic components were frozen to the reddening and column density values from Schlafly & Finkbeiner (2011), Willingale et al. (2013), respectively. In the analysis, we found consistent results between Milky Way, Small Magellanic Cloud (SMC), and Large Magellanic Cloud dust extinction laws; therefore we only report the fits using the SMC dust extinction law.

Due to the uncertain contribution to the XRT WT spectra by the dust rings, we extracted WT spectra using the 5–20 pixel annular extraction region identified in Appendix B for the spectrum for the early SED, and a 10 pixel radius circular extraction region for the later time SED, chosen to minimize the fraction of dust scattered emission in the extraction region, with a background spectrum taken from a 75–125 pixel annular region.[43] Since the intrinsic $N_{\rm H}$ in the WT fits is sensitive to the dust contamination (see Appendix B and Table 5), we also provide fits using BAT and UVOT alone. The results of the analysis are given in Table 2 and plotted in Figure 5.

Examining the SED at $T_0 + 4.2$ ks including BAT, XRT, and UVOT data, we find that a broken power law is preferred, with the *F*-test finding a statistical improvement of $\gg 5\sigma$. The break energy required is at ∼7 keV. At the same epoch, excluding the XRT data, we find again a broken power-law model is preferred, with the *F*-test suggesting the improvement is $>3\sigma$. The photon index for the broken power-law model is consistent with the fits including the XRT spectral files. However, the intrinsic dust extinction is lower: 0.23 ± 0.05 mag compared to 0.51 ± 0.03 mag including all data. Not surprisingly, excluding the XRT data greatly increases the uncertainty in the break frequency.

For the SED at $T_0 + 43$ ks, a broken power law is again preferred, with the *F*-test suggesting a break is statistically required at $>3\sigma$. The break frequency remains in the X-ray bandpass, with evidence for a decline in energy over this period. The fits still prefer a significant host galaxy reddening,

[42] We used ZDUST for both the Galaxy and host galaxy dust components, but with the redshift set to zero for the Milky Way dust component.
[43] See https://www.swift.ac.uk/analysis/xrt/backscal.php.

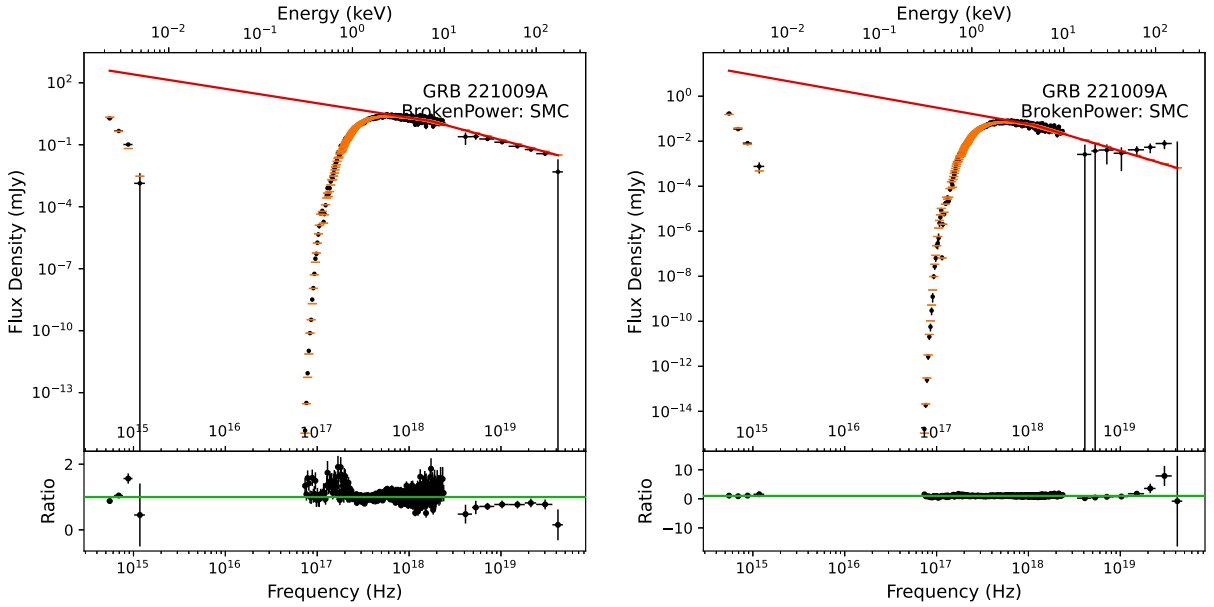

Figure 5. Spectral energy distributions at $T_0 + 4.2$ ks and $T_0 + 43$ ks, containing BAT, XRT, and UVOT data. The top panel displays the best-fit unabsorbed broken power-law model (red) together with the data (black) and the data folded with the model (orange). The bottom panel shows the ratio between the data and the model folded through the instrument response.

Table 2
Fits to the Two Spectral Energy Distributions, at $T_0 + 4.2$ ks and $T_0 + 43$ ks, Built Using UV–Optical (U), X-Ray (X), and Gamma-Ray (B) Data

SED	Model	$N_{\rm H,X,host}$ (10^{22} cm^{-2})	$E(B-V)_{\rm host}$ (mag)	Γ	$E_{\rm bk}$ (keV)	χ^2 (d.o.f)	Null Hypothesis Probability
B+U 4.2 ks	POW	⋯	0.26 ± 0.05	1.74 ± 0.02	⋯	16 (9)	7.3×10^{-2}
B+U 4.2 ks	BKPOW	⋯	0.23 ± 0.05	$1.70^{+0.03}_{-0.12}$	$33.6^{+16.1}_{-28.6}$	4 (8)	8.4×10^{-1}
B+X+U 4.2 ks	POW	1.75 ± 0.03	1.04 ± 0.02	1.93 ± 0.01	⋯	1372 (681)	6.9×10^{-49}
B+X+U 4.2 ks	BKPOW	1.35 ± 0.03	0.51 ± 0.03	1.69 ± 0.01	6.8 ± 0.3	861 (680)	2.7×10^{-6}
B+U 43 ks	POW	⋯	0.38 ± 0.06	1.89 ± 0.04	⋯	14 (9)	1.2×10^{-1}
B+U 43 ks	BKPOW	⋯	0.38 ± 0.06	1.39 ± 0.04	$7.3^{+17}_{-7.3} \times 10^{-4}$	14 (8)	8.3×10^{-2}
B+X+U 43 ks	POW	1.27 ± 0.03	0.49 ± 0.03	1.83 ± 0.01	⋯	778 (678)	4.2×10^{-3}
B+X+U 43 ks	BKPOW	1.14 ± 0.08	0.28 ± 0.03	1.72 ± 0.02	4.5 ± 0.2	748 (677)	3.0×10^{-2}

Note. Both epochs were fit with a power-law (POW) continuum and a broken power-law (BKPOW) continuum, accounting for Galactic and host galaxy gas and dust. The columns are time of the SED; model; host galaxy equivalent column density $N_{\rm H,X,host}$; host galaxy reddening, $E(B-V)_{\rm host}$; power-law photon index or the first photon index of the broken power-law model Γ (Γ_2 is fixed to be $\Gamma + 0.5$); break energy for the broken power-law spectral models $E_{\rm bk}$; χ^2, degrees of freedom (d.o.f); and the null hypothesis probability.

but the exact value of $E(B-V)_{\rm host}$ again varies depending on the inclusion or exclusion of the XRT data.

To summarize, both at $T_0 + 4.2$ ks and $T_0 + 43$ ks, we find strong evidence favoring a broken power-law model, with the lower energy photon index $\Gamma \approx 1.7$. Both epochs favor a break energy in the X-ray bandpass, and a modest amount of intrinsic absorption and/or reddening in the host galaxy: $E(B-V)_{\rm host} \approx 0.3$–$0.5$ mag; $N_{\rm H} \approx (1.1$–$1.4) \times 10^{22}$ cm^{-2}. These results are broadly consistent with those reported in Levan et al. (2023), Kann et al. (2023). More precise constraints, however, are precluded due to the complications resulting from the dust scattering echoes.

Finally, we note that, while we have assumed here that any spectral break must be due to the synchrotron cooling frequency (and thus $\Delta\beta = 0.5$), alternative explanations for complex spectral behavior aside from standard forward shock afterglow evolution have been suggested previously in the literature. For example, the possibility of dust destruction by the intense early-time UV flash could lead to spectral evolution due to a time-variable column density (Morgan et al. 2014). Alternatively, thermal emission has been claimed in the X-ray spectra of a number of previous GRB afterglows (e.g., Campana et al. 2006). Given the complexities induced by the dust echoes, however, a detailed investigation of the X-ray spectral evolution is beyond the scope of this work.

3.3. Light Curve

The combined X-ray and UV–optical light curves of GRB 221009A are shown in Figure 2 (top and bottom panels, respectively). The XRT, MAXI, and NICER measurements are placed in a common bandpass from 0.3–10.0 keV. The BAT survey mode data, however, are *not* extrapolated to this band and instead plotted from 14 to 195 keV—due to the inference

of a spectral break below this band (Section 3.2), these points are instead meant to be illustrative.

While soft X-ray observations of the afterglow did not begin until $T_0 + 2.5$ ks, the light curve clearly lacks signatures of the canonical X-ray afterglow behavior at early times, including the prompt decay phase, the plateau phase, and any prominent flaring (Nousek et al. 2006). This relatively simple monotonic decay has been noted previously in other GRBs detected at high ($\geqslant$GeV) energies (Yamazaki et al. 2020).

We fit the joint 0.3–10.0 keV (XRT+MAXI+NICER) X-ray light curve using the Markov Chain Monte Carlo software package EMCEE (Foreman-Mackey et al. 2019). An additional fixed fractional error was included as a nuisance parameter to account for cross-calibration uncertainty. We find a broken power-law model is strongly preferred over a single power law, although still formally a more complex behavior is indicated. The best-fit parameters for the broken power-law model are $\alpha_{\rm X,1} = -1.498 \pm 0.004$, $\alpha_{\rm X,2} = -1.672 \pm 0.008$, and $t_{\rm break,X} = (7.9^{+1.1}_{-1.0}) \times 10^4$ s (68% confidence intervals). The initial MAXI detection at $T_0 + 2.5$ ks clearly indicates a shallower decay at early times ($T_0 + \lesssim 3.3$ ks), while a late-time excess ($T_0 + 2$ Ms) may indicate some energy injection (e.g., Zhang et al. 2006), or alternatively could be due to contamination from, e.g., an unrelated foreground object.

For the UV–optical data, we constructed a combined single-band light curve following the procedure outlined in Oates et al. (2009). We then fit this light curve using the identical procedure described above for the X-ray data (including the cross-calibration nuisance parameter). We find that a single power-law model and broken power-law model provide comparable quality fits to the data—the statistically preferred model depends sensitively on how late-time ($>10^5$ ks) measurements are included in the fit. The best-fit index derived for the single power-law model is $\alpha_{\rm O} = -1.13 \pm 0.01$, while for the broken power-law model the parameters are $\alpha_{\rm O,1} = -0.98^{+0.11}_{-0.05}$, $\alpha_{\rm O,2} = -1.31^{+0.05}_{-0.07}$, and $t_{\rm break,O} = (2.2^{+1.7}_{-1.1}) \times 10^4$ s. Regardless of the model selected, the UV–optical light curve clearly declines more slowly than the X-ray emission. Given the large foreground extinction, these wavelengths are unaffected by contamination from an emerging supernova or an underlying host galaxy, and thus this accurately reflects the afterglow behavior.

4. Discussion

4.1. Comparison with Previous GRBs

The top panel of Figure 6 plots the observed 0.3–10.0 keV flux light curve of GRB 221009A, overplotted on the entire sample of XRT light curves since the Swift launch (all uncorrected for absorption). At the time of the first XRT observations, GRB 221009A is approximately an order of magnitude brighter than any previous X-ray afterglow. Put differently, forming the distribution of X-ray afterglow flux at $T_0 + 4.5$ ks (a time selected to minimize the number of events requiring interpolation due to orbital gaps in light-curve coverage), GRB 221009A falls 5.5σ above the mean.

However, GRB 221009A is also one of the nearest GRBs detected since the launch of Swift—12 events (out of $\approx$400) have lower redshifts reported in the online Swift GRB Table.[44] To compare to the intrinsic properties of the X-ray afterglow sample, we converted the observed count-rate light curve into intrinsic luminosity in the 0.3–10 keV energy band in the GRB comoving frame. The luminosity in a given bin is given by the following:

$$L = 4\pi D_L^2 R C_u k \quad (2)$$

where D_L is the luminosity distance (749.3 Mpc), R is the measured 0.3–10 keV count rate (in the observer frame), C_u is the conversion from count rate to unabsorbed 0.3–10 keV flux (also in the observer frame) obtained from the spectral fits above (Section 2.2), and k is the k-correction of Bloom et al. (2001), which corrects from observed 0.3–10 keV flux to the 0.3–10 keV flux in the GRB comoving frame. To calculate k, we assume the spectrum is an unbroken power law with the photon index $\Gamma = 1.8$. The time axis must also be corrected to the observer frame, by dividing the time by $1 + z = 1.151$. The resultant light curve is shown in the bottom panel of Figure 6.

While the lack of early-time observations somewhat complicates the comparison, it is clear that GRB 221009A is at the high end of the X-ray afterglow luminosity distribution (1.8σ above the mean). But unlike when considering this comparison in flux space, GRB 221009A is by no means an outlier. Rather we conclude that the exceptional observed brightness of the X-ray afterglow of GRB 221009A results from the combination of being very nearby and very intrinsically luminous: while neither the distance nor the luminosity are unprecedented, together they make GRB 221009A unique among the Swift afterglow sample.

Comparing GRB 221009A to the broader population of UV–optical afterglows is further complicated by the large (and uncertain) line-of-sight extinction, both foreground and in the host galaxy. With $m_U = 17.59^{+0.13}_{-0.12}$ mag at $T_0 + 3574$ s, GRB 221009A is significantly fainter than the brightest UVOT-detected afterglows, such as GRB 080319B ($m_U \approx 15.4$ mag; Bloom et al. 2009; Racusin et al. 2009) and GRB 130427A ($m_U \approx 13.9$ mag; Maselli et al. 2014) at comparable observer-frame times post-burst. But even applying only a correction for foreground (i.e., Milky Way) extinction of $A_U \approx 6.8$ mag (Schlafly & Finkbeiner 2011), the UV–optical emission from GRB 221009A would likely have been the brightest observed to date had it occurred at high Galactic latitude (see also Kann et al. 2023).

If we adopt $E(B-V)_{\rm host} = 0.4$ mag and an SMC-like extinction law (Section 3.2), we infer a U-band host extinction of 1.8 mag. Neglecting k-corrections (which are likely to be much smaller than the uncertainty in the extinction correction), we find an absolute magnitude of $M_U \approx -29.3$ mag (AB). Comparing to Figure 7 in Perley et al. (2014), we find that the UV–optical light curve of GRB 221009A occupies a similar location in luminosity space as the X-ray afterglow: toward the most luminous end, but entirely consistent with the existing distribution.

4.2. Astrophysical Rate

Although Swift was behind the Earth at T_0, we use the GBM light curve and spectrum (S. Lesage et al. 2023, in preparation) to estimate what GRB 221009A would have looked like to the BAT, as well as to determine the occurrence rate of such events. Adopting the time-averaged spectrum of the main pulse from $T_0 + 218.5$–277.9 s (10–1000 keV fluence of 8.293×10^{-2} erg cm^{-2}), we derive a BAT (15–150 keV band) fluence

[44] See https://swift.gsfc.nasa.gov/archive/grb_table.

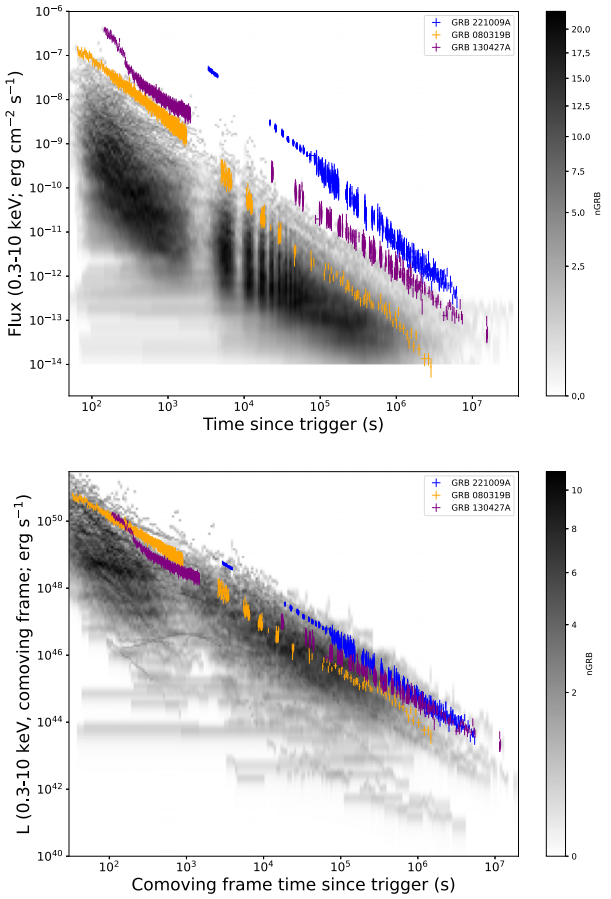

Figure 6. A comparison of GRB 221009A with all of those observed by XRT. The gray scales indicate the number of GRBs in each (time, brightness) bin; the blue light curve is GRB 221009A, with two notable bright GRBs, GRB 130427A (purple) and GRB 080319B (orange) shown for comparison. Top: observer frame, 0.3–10 keV observed flux light curves. Bottom: comoving-frame, 0.3–10 keV intrinsic (unabsorbed) luminosity light curves; the gray-scale sample data includes only those GRBs with published redshifts.

of 1.86×10^{-2} erg cm^{-2} s^{-1} and an average flux of 3.13×10^{-4} erg cm^{-2} s^{-1}. This fluence from the main pulse alone is 50 × higher than the largest fluence detected to date by BAT (GRB 130427A; Maselli et al. 2014).

At $z = 0.151$, the 15–150 keV (rest-frame) isotropic prompt energy release for the main pulse is $E_{\gamma,\rm iso} = 9 \times 10^{53}$ erg. We employ the 15–150 keV energy range to facilitate a direct comparison with the entire population of BAT GRBs with measured redshifts.

To estimate the relative occurrence rate of such an energetic event, we compare GRB 221009A with the intrinsic long GRB luminosity function derived in Lien et al. (2014). We consider only the main pulse, as this dominates the burst energetics, and it is difficult to ascertain when the prompt emission ends, given the afterglow was bright enough to trigger the BAT at $T_0 +$ 3.4 ks.

We randomly generated 10^4 GRBs using the intrinsic GRB rate and luminosity distribution in Lien et al. (2014), and each simulated burst was randomly assigned a pulse structure drawn from the real BAT GRB sample. We calculated the $E_{\gamma,\rm iso}$ of these simulated bursts, and found that only one burst had an energy release (slightly) higher than the main pulse of GRB 221009A. Therefore, we conclude only $\sim 1/10^4$ long GRBs are as energetic as GRB 221009A.

Using this value, we crudely estimate the rate at which such energetic GRBs are detectable by BAT:

$$N_{\rm BAT} \approx R_{\rm GRB}\, f_{\rm Eiso}\, f_{\rm FOV}\, f_{\rm survey} = 0.06 \text{ yr}^{-1}, \quad (3)$$

where $R_{\rm GRB}$ is the intrinsic all-sky long-GRB rate from Lien et al. (2014), $f_{\rm Eiso} = 1.0 \times 10^{-4}$ is the fraction of GRBs in this intrinsic sample that have $E_{\gamma,\rm iso}$ larger than GRB 221009A, $f_{\rm FOV} = 1/6$ is the fraction of sky covered by the BAT field of view, and $f_{\rm survey} = 0.8$ is the fraction of time BAT is able to trigger on GRBs (neglecting spacecraft slews, SAA passage, etc.). In other words, we need to wait $\sim 1/0.06 = 17$ yr for an event like the main pulse of GRB 221009A to occur in the BAT field of view.

We emphasize, however, that the above estimate simply indicates that BAT should have detected ∼1 GRB more energetic than GRB 221009A over its lifetime, *independent of distance*. But in addition to being highly energetic, GRB 221009A is also one of the most nearby GRBs detected by Swift. To estimate the intrinsic (volumetric) rate of comparable events, we utilize the BAT trigger simulator (Lien et al. 2014) to calculate the detectability of the prompt emission at different redshifts under different representative geometries. The full details of the simulation are provided in Appendix G.

Using this framework, we derive an upper limit on the local volumetric rate of GRB 221009A–like events of $R_{\rm GRB,comov}(z = 0) \leqslant 6.1 \times 10^{-4}$ Gpc^{-3} yr^{-1}. Integrating this flat comoving rate from $z = 0$, to $z = 10$, we obtain an upper limit on the all-sky rate of such events of $\leqslant 0.5$ yr^{-1}. Comparing to the all-sky intrinsic long GRB rate of ∼4571 yr^{-1} in Lien et al. (2014), the fraction of GRB 221009A–like events is roughly $0.5/4571 \leqslant 1.0 \times 10^{-4}$, which is similar to the relative rate derived above.

Even more remarkable, we can use these results to derive the rate of GRB 221009A–like GRBs within the volume out to $z = 0.151$ (1.1 Gpc^{-3}). **This implies we would need to wait over ≈10^3 yr to detect another GRB 221009A–like event within this volume.** The combination of the large energy release and the small distance make GRB 221009A truly a once in a lifetime phenomenon.

4.3. The Nature of Energetic GRBs

Interpreting GRB 221009A in the context of the standard afterglow synchrotron model (e.g., Sari et al. 1998) presents a number of challenges, in particular if the X-ray and optical emission is assumed to arise from a common origin (see Ghisellini et al. 2007; De Pasquale et al. 2009). To begin with, the broadband spectral fitting performed in Section 3.2 strongly favors the presence of a spectral break around the soft X-ray band, with the change in spectral slope being consistent with the cooling frequency ν_c. However, if we adopt relatively standard afterglow parameters ($\epsilon_B = 0.01$, $p = 2.5$, $\eta_\gamma = 0.15$), then we find that a cooling frequency ≈5 keV (10^{18} Hz) at ≈0.1 day post-trigger implies a jet expanding into an extremely low density circumburst environment: $n_0 \approx 10^{-3}$ cm^{-3} for a constant-density (interstellar-medium-like) environment. Such low densities have been inferred previously for highly energetic events (e.g., Cenko et al. 2011), but this remains difficult to reconcile with the massive star progenitors of long GRBs.

Furthermore, standard afterglow closure relations (e.g., Racusin et al. 2009) are unable to reproduce the observed spectral and temporal power-law indices. For example, the broadband SED fits presented in Section 3.2 find an optical spectral index $\beta_O \approx 0.7$. This is consistent with the temporal decay observed for a jet expansion into a constant-density medium ($\alpha_0 \approx 1.1$; $p \approx 2.4$). However, this would predict a significantly shallower temporal decay in the X-rays ($\alpha_X \approx 1.3$) than what is observed. While expansion into a wind-like medium would predict a steeper X-ray temporal decay, the optical emission is inconsistent with this picture.

Given the exceptionally large $E_{\gamma,\rm iso}$, GRB 221009A requires a narrow opening angle (and hence an early jet break time) in order to be compatible with the geometry-corrected energy release inferred from the pre-Swift sample (e.g., Frail et al. 2001). Assuming an efficiency of ≈15% in converting bulk kinetic energy into prompt γ-ray emission, a beaming-corrected energy release of $\leqslant 10^{52}$ erg requires an opening angle of $\theta_j \lesssim 4°$. For a top-hat jet expanding into a constant-density medium, this implies a jet break time of the following:

$$t_j \leqslant 3.5\left(\frac{n_0}{0.1\ \rm cm^{-3}}\right)^{-1/3}\ \rm days \quad (4)$$

where n_0 is the circumburst density in units of $0.1\ \rm cm^{-3}$ (Sari et al. 1999). Note that, due to the $-1/3$ exponent, this result is relatively insensitive to the exact value of the circumburst density.

With X-ray coverage extending out to $T_0 + 70$ days, the Swift+MAXI+NICER X-ray light curve is more than adequate to search for such a geometric signature. But out to late times, the temporal decay does not steepen beyond $\alpha_X = 1.7$, significantly shallower than the $\alpha > 2$ behavior anticipated for a simple on-axis top-hat jet.

The X-ray afterglow steepening observed at $T_0 + 8 \times 10^4$ s could conceivably be attributed to a jet break (see also D'Avanzo et al. 2022). In this case, the corresponding jet would indeed be extremely narrow, with an implied opening angle of ≈2°. However, as described above, the post-break decay index is significantly shallower than expected for an on-axis top-hat jet. Interestingly, similar behavior was observed in GRB 130427A and attributed to time-variable microphysical parameters (Maselli et al. 2014). One alternative explanation is a complex angular structure for the jet (i.e., compared to the simple top-hat model assumed above, with a constant energy as a function of angle). The presence of energetic material outside the jet "edges" would naturally account for the shallower decline initially (e.g., O'Connor et al. 2023). However, eventually when viewed sufficiently far off-axis, the decay should steepen (assuming the material is still relativistic), something not observed in the X-ray light curve out to $T_0 + 70$ days. A detailed exploration of the jet structure would require additional multiwavelength observations, in particular radio coverage, and is thus beyond the scope of this work.

5. Conclusions

Here we present the combined Swift, MAXI, and NICER observations of GRB 221009A, spanning from $T_0 + 2.5$ ks to $T_0 + 73$ days and from UV to hard X-ray energies, providing the opportunity to study the prolonged afterglow in exquisite detail. The primary conclusions are as follows:

1. Through dust echo tomography, we identify a series of dust clouds along the line of sight in our galaxy at distances ranging from 200 pc to beyond 10 kpc (i.e., well above the Galactic disk). As such, the dust echo from GRB 221009A proves that echo tomography is acutely sensitive to small dust concentrations at large distances that are not easily measurable with other techniques.
2. The X-ray afterglow of GRB 221009A is more than an order of magnitude brighter at $T_0 + 4.5$ ks (in terms of measured flux) than any previous GRB observed by Swift. However, the intrinsic X-ray afterglow luminosity is at the high end, but consistent with, the distribution of Swift GRBs with redshifts. Thus, GRB 221009A is unique because it is both luminous and very nearby (by GRB standards).
3. We calculate the rate of GRB 221009A–like events (i.e., GRBs with prompt emission as energetic/luminous as that inferred by the GBM). We find that only ∼1 in 10^4 GRBs has an $E_{\gamma,\rm iso}$ comparable to GRB 221009A. When factoring in the distance, we find that the rate of GRBs as energetic and nearby as GRB 221009A is $\lesssim$1 per 1000 yr.
4. From the extensive multiwavelength data sets, we find that the afterglow emission from GRB 221009A is not well described by standard synchrotron afterglow theory. In particular, the break observed in the X-ray light curve at $T_0 + 79$ ks is inconsistent with a jet break from an on-axis top-hat jet. Either the jet structure is more complex, with significant power outside the jet core, or GRB 221009A is not narrowly collimated. The latter scenario would have profound implications for the energy budget of the event.

While GRB 221009A disappeared behind the Sun for most observatories at ≈70 days post-burst, the X-ray and radio afterglow are still anticipated to be easily detectable after the field becomes visible again in ≈2023 February. Coupled with the exquisite multiwavelength data collected from radio to VHE gamma rays, the broadband story of this exceptional event will continue to unfold over the coming months, years, and (perhaps) decades.

We acknowledge the use of public data from the Swift data archive. This work made use of data supplied by the UK Swift Science Data Centre at the University of Leicester. This research has made use of MAXI data provided by RIKEN, JAXA, and the MAXI team.

P.A.E., A.P.B., K.L.P., N.P.M.K. acknowledge UKSA funding. The material is based upon work supported by NASA under award number 80GSFC21M0002. Swift at Penn State is supported by NASA contract NAS5-00136. E.A., M.G.B., A.D., P.D.A., A.M., M.P., B.S., S.C., and G.T. acknowledge funding from the Italian Space Agency, contract ASI/INAF n. I/004/11/4. P.D.A. acknowledges support from PRIN-MIUR 2017 (grant 20179ZF5KS). G.Y. acknowledges the support of NASA Postdoctoral Program at the Goddard Space Flight Center, administered by Oak Ridge Associated Universities under contract with NASA. S.H. acknowledges support from NSF grant AST2205917. Part of this work was financially supported by Grants-in-Aid for Scientific Research 21K03620 (H.N.), 22H01276 (T.M., H.N., M.Se.), and 17H06362 (N.Ka., H.N., T.M., M.Se.) from the Ministry of Education, Culture, Sports, Science, and Technology (MEXT) of Japan.

We acknowledge the hard work of the Swift and NICER operations teams in performing these observations.

Facilities: Swift (BAT, XRT, and UVOT), MAXI, NICER.

Software: HEASOFT (NASA High Energy Astrophysics Science Archive Research Center (Heasarc), 2014); BATANALYSIS (T. Parsotan et al. 2023, in preparation); XSPEC (Arnaud 1996); ASTROPY (Astropy Collaboration et al. 2013); EMCEE (Foreman-Mackey et al. 2019).

Appendix A
BAT Survey Mode and Mosaic Flux Measurements

Details of the flux measurements and upper limits obtained from the Swift BAT survey mode data are shown in Table 3, and the results of the daily mosaicing are presented in Table 4.

Table 3
BAT Survey Observations of GRB 221009A

Obs ID	Pointing ID	$T_{start} - T_0$ (ks)	UTC Time	Exposure (ks)	14–195 keV Flux (erg cm^{-2} s^{-1})	Photon Index
03111868007	20222810634	−110.5	2022 Oct 8 06:34:32	0.661	$<1.11 \times 10^{-8}$	⋯
	20222821110	−7.6	2022 Oct 9 11:10:19	0.373	$<1.55 \times 10^{-8}$	⋯
00015314118	20222820117	−43.2	2022 Oct 9 01:17:08	0.924	$<6.33 \times 10^{-9}$	⋯
00046390010	20222820135	−42.1	2022 Oct 9 01:34:40	0.172	$<3.34 \times 10^{-8}$	⋯
00015314119	20222820626	−24.6	2022 Oct 9 06:26:19	0.900	$<6.36 \times 10^{-9}$	⋯
00015357004	20222820921	−14.1	2022 Oct 9 09:21:28	0.544	$<1.42 \times 10^{-8}$	⋯
00011105067	20222821046	−9.1	2022 Oct 9 10:46:08	1.344	$<1.36 \times 10^{-8}$	⋯
00015314120	20222821248	−1.7	2022 Oct 9 12:48:26	0.846	$<7.14 \times 10^{-9}$	⋯
01126854000	20222821422	3.9	2022 Oct 9 14:22:05	0.627	$3.22^{+0.38}_{-0.37} \times 10^{-8}$	$2.13^{+0.19}_{-0.19}$
01126853001	20222821917	21.6	2022 Oct 9 19:17:08	0.500	$2.61^{+0.93}_{-0.86} \times 10^{-9}$	$1.81^{+0.44}_{-0.44}$
01126853003	20222822027	25.8	2022 Oct 9 20:26:45	0.900	$2.44^{+0.66}_{-0.62} \times 10^{-9}$	$2.31^{+0.52}_{-0.51}$
00015314121	20222822047	27.0	2022 Oct 9 20:46:57	0.755	$3.01^{+1.11}_{-1.02} \times 10^{-9}$	$1.53^{+0.57}_{-0.54}$
01126853004	20222822156	31.1	2022 Oct 9 21:55:37	1.744	$1.73^{+0.55}_{-0.5} \times 10^{-9}$	$1.85^{+0.49}_{-0.48}$
	20222822332	36.9	2022 Oct 9 23:31:40	1.500	$<4.09 \times 10^{-9}$	⋯
	20222830129	43.9	2022 Oct 10 01:29:08	1.073	$<4.76 \times 10^{-9}$	⋯
	20222830243	48.4	2022 Oct 10 02:43:05	1.742	$<3.82 \times 10^{-9}$	⋯
	20222830417	54.0	2022 Oct 10 04:16:45	1.738	$<3.74 \times 10^{-9}$	⋯
	20222830754	67.0	2022 Oct 10 07:53:52	0.914	$<5.05 \times 10^{-9}$	⋯
	20222830934	73.0	2022 Oct 10 09:34:21	0.514	$<6.78 \times 10^{-9}$	⋯
	20222831234	83.8	2022 Oct 10 12:33:38	1.314	$<4.61 \times 10^{-9}$	⋯
	20222831354	88.6	2022 Oct 10 13:53:49	1.183	$<4.81 \times 10^{-9}$	⋯
	20222831531	94.4	2022 Oct 10 15:30:56	0.900	$<5.34 \times 10^{-9}$	⋯
	20222831550	95.6	2022 Oct 10 15:50:56	0.543	$<6.53 \times 10^{-9}$	⋯
	20222831704	100.0	2022 Oct 10 17:04:26	1.679	$<3.76 \times 10^{-9}$	⋯
03111808004	20222830447	55.8	2022 Oct 10 04:46:38	0.594	$<5.99 \times 10^{-9}$	⋯
00033349157	20222830906	71.3	2022 Oct 10 09:05:56	1.655	$<3.68 \times 10^{-9}$	⋯
00015314124	20222831417	90.0	2022 Oct 10 14:17:05	0.807	$<7.28 \times 10^{-9}$	⋯
01126853005	20222831837	105.6	2022 Oct 10 18:37:15	1.500	$<3.80 \times 10^{-9}$	⋯
00015314125	20222831904	107.2	2022 Oct 10 19:03:48	0.704	$<7.11 \times 10^{-9}$	⋯
01126853006	20222832022	111.9	2022 Oct 10 20:22:19	1.500	$<4.07 \times 10^{-9}$	⋯
	20222832147	117.0	2022 Oct 10 21:47:19	0.900	$<5.17 \times 10^{-9}$	⋯
	20222832204	118.2	2022 Oct 10 22:07:19	0.299	$<8.71 \times 10^{-9}$	⋯
	20222840108	129.1	2022 Oct 11 01:08:33	0.839	$<5.31 \times 10^{-9}$	⋯
	20222840233	134.2	2022 Oct 11 02:33:30	0.782	$<5.24 \times 10^{-9}$	⋯
	20222840444	142.0	2022 Oct 11 04:44:25	0.362	$<8.01 \times 10^{-9}$	⋯
	20222840548	145.8	2022 Oct 11 05:47:44	1.499	$<3.98 \times 10^{-9}$	⋯
	20222840735	152.3	2022 Oct 11 07:34:38	1.500	$<4.04 \times 10^{-9}$	⋯
	20222840915	158.3	2022 Oct 11 09:14:53	1.254	$<4.59 \times 10^{-9}$	⋯
	20222841047	163.8	2022 Oct 11 10:47:19	1.453	$<4.26 \times 10^{-9}$	⋯
00015314126	20222840250	135.2	2022 Oct 11 02:50:06	0.806	$<7.35 \times 10^{-9}$	⋯
00015314127	20222840858	157.3	2022 Oct 11 08:58:33	0.899	$<6.83 \times 10^{-9}$	⋯

Note. Upper limits are calculated with an assumed photon index of 1.

Table 4
Swift BAT Daily and Total Mosaics of GRB 221009A

Start Time Bin	End Time Bin	Exposure (ks)	14–195 keV Flux (erg cm^{-2} s^{-1})	Photon Index
2022 Oct 8	2022 Oct 9	0.661	$<2.63 \times 10^{-9}$	...
2022 Oct 9	2022 Oct 10	6.541	$5.05^{+0.29}_{-0.29} \times 10^{-9}$	$2.30^{+0.09}_{-0.09}$
2022 Oct 10	2022 Oct 11	7.710	$6.68^{+2.4}_{-2.1} \times 10^{-10}$	$2.43^{+0.61}_{-0.51}$
2022 Oct 11	2022 Oct 12	4.136	$<6.47 \times 10^{-10}$	...
2022 Oct 8	2022 Oct 12	19.048	$1.90^{+0.17}_{-0.17} \times 10^{-9}$	$2.28^{+0.15}_{-0.14}$

Note. Upper limits are calculated with an assumed photon index of 1.

Appendix B
Swift XRT Dust and Background Subtraction

In WT mode, the Swift XRT CCD is read out in columns, and the spatial information is collapsed to one single dimension. As a result, the *source* region will contain all dust photons *above* and *below* the GRB in terms of CCD position, while the background regions will sample a different vertical slice through the dust rings, with potentially different spectral properties from those in the source region. Furthermore, the columns are summed over the full 600 pixel height of the XRT CCD, but only the central 200 columns are read out, which can make a suitable background region difficult to obtain.

Example time-sliced 1D profiles from the WT-mode data are shown in Figure 7. These suggest that within a 20 pixel source accumulation region, the data are dominated by the source. The profile from the first snapshot of WT data is shown in more detail in Figure 8, along with a fit of the profile expected from a point source; the lower panel shows the difference between the data and model. As the GRB was so bright in this snapshot, the central core profile is suppressed due to pile-up (resulting in a negative residual, which is not shown for clarity); the central 10 columns were subsequently excluded in the spectral extraction to remove the piled-up core. The remaining residuals suggest the scattering echoes contribute ∼10%–15% of the observed count rate in a 5–20 pixel radius extraction region centered on the source; thus the GRB spectral normalization will be overestimated by a similar amount due to the echo contamination in this snapshot.

To investigate the effect of the echo on the subsequent WT-mode flux measurements, we took the PC-mode image from $T_0 + 1.036 - 1.111$ days and summed it in 1D so as to mimic the WT-mode profiles. We did this twice; first using all data, then a second time after removing a model of the central source PSF, which was fit to the innermost 20 pixel radius data. The 1D intensity profiles thus obtained show the sourceless data are approximately flat, with a variation of <25% between the source outer extraction radius and the wings out to 6′. Within the source accumulation region, ∼75% of the events come from the source. Thus, the source light curve is not significantly altered by the variation in the estimated background level obtained from the wings of the 1D profile where the dust dominates.

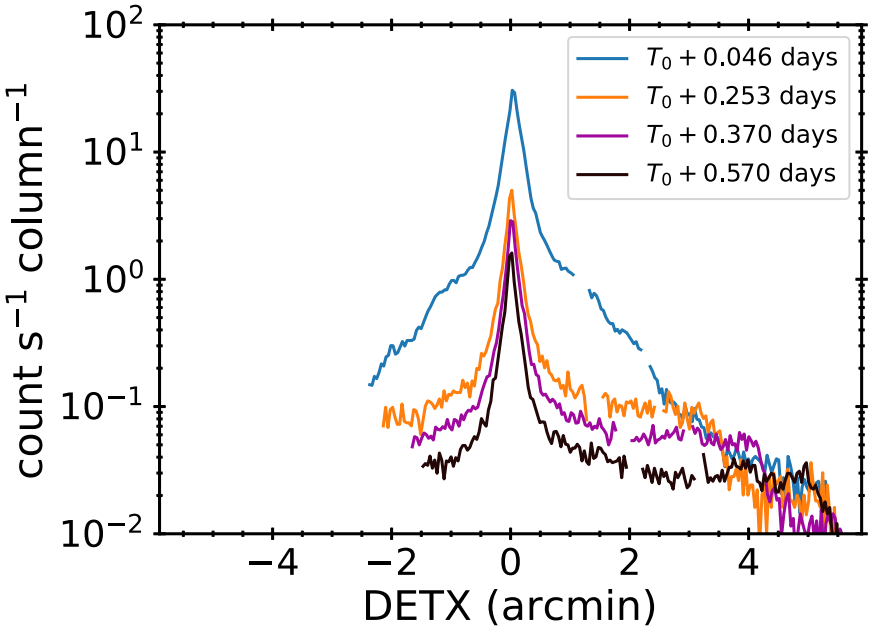

Figure 7. XRT WT-mode 1D PSF profiles as a function of time in the 0.8–5.0 keV band, illustrating the evolution of the echo in the early WT data.

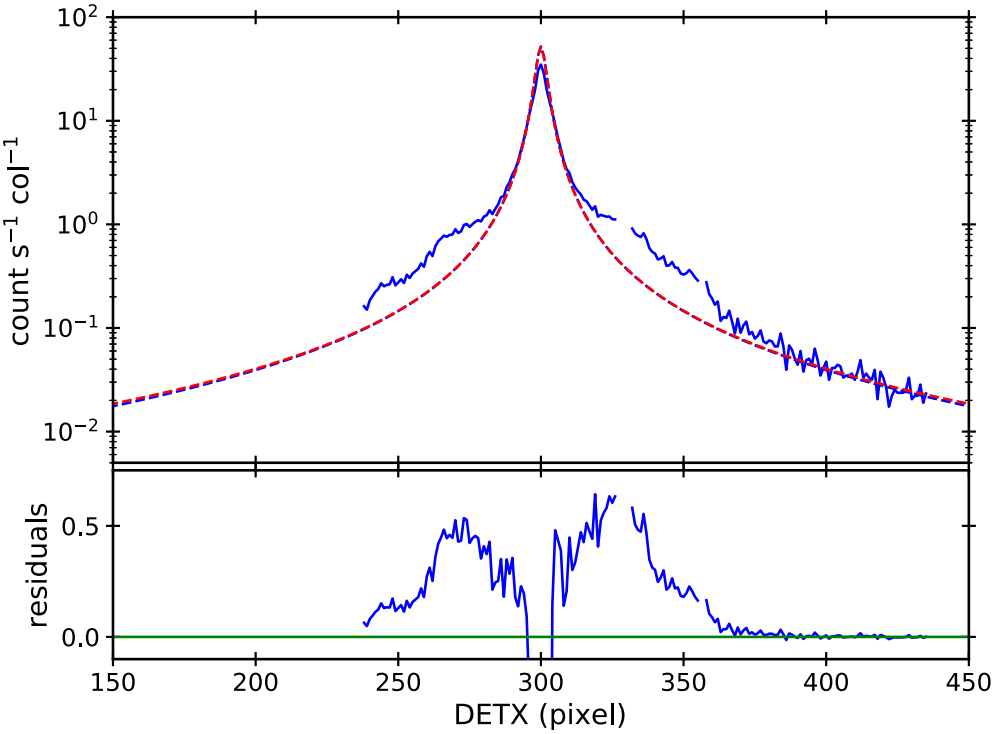

Figure 8. Upper panel: XRT WT-mode 1D PSF profile from the first snapshot of data at $T_0 + 3.4$ ks (solid line) and the modeled point-source profile (dashed line). Lower panel: the data minus model residual.

To determine the impact of dust on the WT-mode spectroscopic data, we used the PC-mode data in ObsID 01126853004, comprising 3.1 ks of data collected between 89 and 101 ks after the Fermi trigger.[45] First we extracted data from a vertical region corresponding to a typical WT-mode background region, and also from a 20 column radius region around the source, excluding the source itself. The spectrum of the dust in the source columns is visibly slightly harder than that in the background region; fitting an absorbed power law in XSPEC showed the difference to be minimal, however, with the best-fitting parameters varying by less than 6% between the two spectra and comfortably agreeing within their 90% confidence errors. To better quantify the effect of this possible change in dust spectrum between source and background regions, we extracted two spectra from the PC-mode data. The first was taken from a 20 pixel radius circle centered on the source (i.e., with no dust present) with a background spectrum taken from the dust-free region identified above. In the second case, we mimicked WT data, extracting data from the full vertical height of the CCD for regions corresponding to those used in the WT-mode analysis (Figure 9). We fit these two spectra independently in XSPEC using the absorbed power-law

[45] Although the first snapshot from this ObsID started at 68 ks, its on time was only 7.5 s, meaning the exposure effectively started during the second snapshot at 89 ks post trigger.

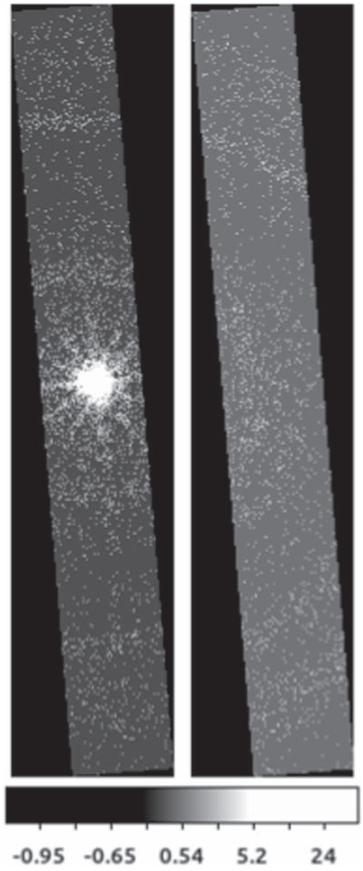

Figure 9. The extracted PC-mode data designed to mimic the WT-mode extraction to investigate the impact of dust. Left: the source region. Right: the background region. The regions are tilted at the roll angle of the spacecraft.

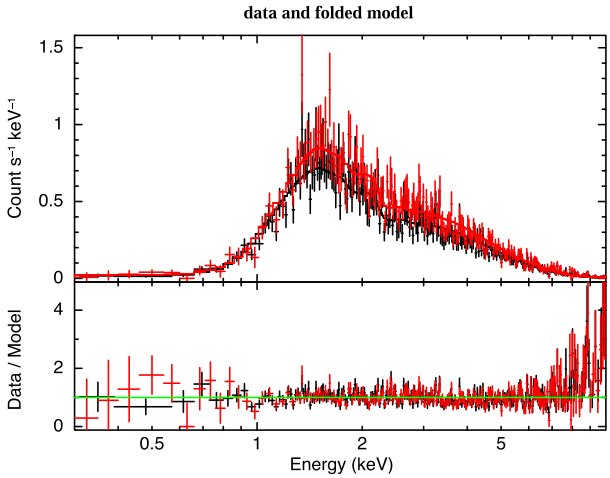

Figure 10. A comparison of a PC-mode spectrum (black), in which dust has been correctly accounted for, and a mimicked WT-mode spectrum (red) of the same data, enabling us to quantify the impact of the dust on the WT-mode data.

model. The results are shown in Table 5 and in Figure 10. While all parameters agree to within their errors, the best-fit photon index is 7% higher (i.e., softer), and the absorption column is 27% higher in the WT-style data. Since these data were gathered when the source was fainter than in the real WT data (i.e., the impact of dust contamination is at its worst in this experiment), we adopt these percentages as the maximum inaccuracy expected from our WT-mode spectral fits.

Table 5
An Estimate of the Impact of Dust on the WT-mode Spectral Fit Results; See Text for Details

Parameter	PC Result	Pseudo-WT Result	Percentage Difference[a]
$N_{\rm H}$ (10^{22} cm^{-2})	1.1 ± 0.2	1.4 ± 0.2	27%
Photon index	1.47 ± 0.08	1.57 ± 0.09	7%
Flux (0.3–10 keV, 10^{-10} erg cm^{-2} s^{-1})	1.64 ± 0.06	1.74 ± 0.06	6%

Note.
[a] (PC-WT)/PC.

Appendix C
UVOT Afterglow Photometry

The final photometry measured for GRB 221009A is displayed in Table 6.

Table 6
Swift UVOT Observations

$T_{\rm mid} - T_0$ (ks)	Half Exposure (s)	Magnitude	Flux (erg cm^{-2} s^{-1} Å^{-1})	Filter	S/N
3.4	25	$16.743^{+0.051}_{-0.048}$	$9.64 \pm 0.44 \times 10^{-16}$	*white*	21.956
3.5	30	$16.762^{+0.046}_{-0.045}$	$9.48 \pm 0.40 \times 10^{-16}$	*white*	23.877
3.5	20	$16.726^{+0.057}_{-0.054}$	$9.80 \pm 0.50 \times 10^{-16}$	*white*	19.698
3.8	10	$16.71^{+0.097}_{-0.089}$	$9.94 \pm 0.85 \times 10^{-16}$	*white*	11.664
4.0	10	$16.958^{+0.103}_{-0.094}$	$7.91 \pm 0.72 \times 10^{-16}$	*white*	11.024
4.1	75	$16.972^{+0.075}_{-0.07}$	$7.81 \pm 0.52 \times 10^{-16}$	*white*	15.078
4.4	10	$16.976^{+0.104}_{-0.095}$	$7.78 \pm 0.71 \times 10^{-16}$	*white*	10.976
21.9	246	$18.803^{+0.063}_{-0.06}$	$1.45 \pm 0.08 \times 10^{-16}$	*white*	17.686
44.9	76	$19.862^{+0.166}_{-0.144}$	$5.45 \pm 0.77 \times 10^{-17}$	*white*	7.065
61.2	408	$20.1^{+0.085}_{-0.079}$	$4.38 \pm 0.33 \times 10^{-17}$	*white*	13.261
120.0	14,394	$21.152^{+0.079}_{-0.074}$	$1.66 \pm 0.12 \times 10^{-17}$	*white*	14.176
152.3	17,859	$21.655^{+0.099}_{-0.09}$	$1.05 \pm 0.09 \times 10^{-17}$	*white*	11.522
198.5	23,982	$21.599^{+0.21}_{-0.176}$	$1.10 \pm 0.19 \times 10^{-17}$	*white*	5.685
258.6	31,606	$21.987^{+0.19}_{-0.162}$	$7.71 \pm 1.24 \times 10^{-18}$	*white*	6.218
306.9	6602	$22.574^{+0.324}_{-0.249}$	$4.49 \pm 1.16 \times 10^{-18}$	*white*	3.872
436.1	49,190	$22.703^{+0.486}_{-0.334}$	$3.99 \pm 1.44 \times 10^{-18}$	*white*	2.773
585.3	71,725	$22.688^{+0.543}_{-0.36}$	$4.04 \pm 1.59 \times 10^{-18}$	*white*	2.541
754.3	91,946	$22.594^{+0.573}_{-0.373}$	$4.41 \pm 1.81 \times 10^{-18}$	*white*	2.440
971.9	120,245	>22.625	$<4.28 \times 10^{-18}$	*white*	⋯
1251.6	154,713	>22.882	$< 3.38 \times 10^{-18}$	*white*	⋯
1701.2	192,141	>22.836	$< 3.52 \times 10^{-18}$	*white*	⋯
2087.8	137,716	>23.166	$< 2.60 \times 10^{-18}$	*white*	⋯
3940.8	432,429	>23.602	$< 1.74 \times 10^{-18}$	*white*	⋯
3.4	5	$15.463^{+0.162}_{-0.141}$	$2.44 \pm 0.34 \times 10^{-15}$	*v*	7.210
3.9	10	$15.538^{+0.125}_{-0.112}$	$2.28 \pm 0.25 \times 10^{-15}$	*v*	9.220
4.2	114	$15.729^{+0.094}_{-0.086}$	$1.91 \pm 0.16 \times 10^{-15}$	*v*	12.072
4.4	10	$15.893^{+0.145}_{-0.128}$	$1.64 \pm 0.21 \times 10^{-15}$	*v*	7.995
38.2	412	$18.152^{+0.077}_{-0.072}$	$2.05 \pm 0.14 \times 10^{-16}$	*v*	14.642
55.3	412	$18.755^{+0.11}_{-0.1}$	$1.18 \pm 0.11 \times 10^{-16}$	*v*	10.375
92.8	8959	$19.427^{+0.123}_{-0.11}$	$6.34 \pm 0.68 \times 10^{-17}$	*v*	9.342
436.6	49,188	>20.443	$< 2.49 \times 10^{-17}$	*v*	⋯
573.7	59,918	$21.082^{+0.698}_{-0.421}$	$1.38 \pm 0.66 \times 10^{-17}$	*v*	2.109
822.1	97,374	>20.64	$< 2.08 \times 10^{-17}$	*v*	⋯
1065.7	122,800	>21.411	$< 1.02 \times 10^{-17}$	*v*	⋯
1372.4	160,437	>21.617	$< 8.44 \times 10^{-18}$	*v*	⋯
1833.6	220,177	>22.032	$< 5.76 \times 10^{-18}$	*v*	⋯
2151.2	74,786	>21.125	$< 1.33 \times 10^{-17}$	*v*	⋯
3940.0	432,472	>21.862	$< 6.74 \times 10^{-18}$	*v*	⋯
3.8	10	$17.062^{+0.144}_{-0.127}$	$9.70 \pm 1.20 \times 10^{-16}$	*b*	8.058
4.0	10	$17.227^{+0.155}_{-0.136}$	$8.34 \pm 1.11 \times 10^{-16}$	*b*	7.495
4.4	92	$17.551^{+0.144}_{-0.127}$	$6.18 \pm 0.77 \times 10^{-16}$	*b*	8.073
44.4	454	$20.268^{+0.145}_{-0.128}$	$5.06 \pm 0.63 \times 10^{-17}$	*b*	7.999
60.3	453	$20.666^{+0.237}_{-0.194}$	$3.51 \pm 0.69 \times 10^{-17}$	*b*	5.100
438.9	52,551	>21.71	$< 1.34 \times 10^{-17}$	*b*	⋯
584.9	71,610	>21.597	$< 1.49 \times 10^{-17}$	*b*	⋯
753.8	92,017	$22.444^{+0.512}_{-0.346}$	$6.82 \pm 2.56 \times 10^{-18}$	*b*	2.662
971.7	120,321	>22.02	$< 1.01 \times 10^{-17}$	*b*	⋯
1251.2	154,869	>22.124	$< 9.16 \times 10^{-18}$	*b*	⋯
1700.9	192,324	>22.229	$< 8.32 \times 10^{-18}$	*b*	⋯
2087.2	137,713	>22.48	$< 6.60 \times 10^{-18}$	*b*	⋯
3849.4	438,307	>22.969	$< 4.21 \times 10^{-18}$	*b*	⋯
3.6	38	$17.592^{+0.129}_{-0.115}$	$3.24 \pm 0.36 \times 10^{-16}$	*u*	8.927
3.7	50	$17.673^{+0.115}_{-0.104}$	$3.01 \pm 0.30 \times 10^{-16}$	*u*	9.933
3.7	37	$17.629^{+0.131}_{-0.117}$	$3.13 \pm 0.36 \times 10^{-16}$	*u*	8.773
3.9	10	$17.882^{+0.309}_{-0.24}$	$2.48 \pm 0.61 \times 10^{-16}$	*u*	4.041
4.4	97	$17.765^{+0.196}_{-0.166}$	$2.77 \pm 0.46 \times 10^{-16}$	*u*	6.043
32.4	415	$20.258^{+0.207}_{-0.174}$	$2.78 \pm 0.48 \times 10^{-17}$	*u*	5.769

Table 6
(Continued)

$T_{\rm mid} - T_0$ (ks)	Half Exposure (s)	Magnitude	Flux (erg cm^{-2} s^{-1} Å^{-1})	Filter	S/N
49.7	414	$20.729^{+0.313}_{-0.243}$	$1.80 \pm 0.45 \times 10^{-17}$	*u*	3.992
95.8	414	$21.106^{+0.438}_{-0.311}$	$1.27 \pm 0.42 \times 10^{-17}$	*u*	3.010
438.8	52,496	>20.903	$< 1.54 \times 10^{-17}$	*u*	⋯
584.7	71,385	>20.647	$< 1.94 \times 10^{-17}$	*u*	⋯
753.5	91,837	>21.678	$< 7.52 \times 10^{-18}$	*u*	⋯
971.4	120,396	>21.285	$< 1.08 \times 10^{-17}$	*u*	⋯
1251.1	154,783	>21.32	$< 1.05 \times 10^{-17}$	*u*	⋯
1700.8	192,285	>21.335	$< 1.03 \times 10^{-17}$	*u*	⋯
2086.9	137,473	>20.098	$< 3.23 \times 10^{-17}$	*u*	⋯
3848.7	438,428	>22.798	$<2.68 \times 10^{-18}$	*u*	⋯
3.9	10	$18.238^{+0.671}_{-0.412}$	$2.02 \pm 0.93 \times 10^{-16}$	*uvw1*	2.168
4.4	97	>19.108	$< 9.06 \times 10^{-17}$	*uvw1*	⋯
31.6	450	>20.175	$< 3.39 \times 10^{-17}$	*uvw1*	⋯
48.8	450	>20.003	$< 3.97 \times 10^{-17}$	*uvw1*	⋯
67.5	450	>20.5	$< 2.51 \times 10^{-17}$	*uvw1*	⋯
92.4	2910	>21.471	$< 1.03 \times 10^{-17}$	*uvw1*	⋯
685.4	269	>20.833	$< 1.85 \times 10^{-17}$	*uvw1*	⋯
1458.7	22,863	>22.436	$< 4.23 \times 10^{-18}$	*uvw1*	⋯
3.9	10	>18.228	$< 2.37 \times 10^{-16}$	*uvm2*	⋯
4.4	97	>18.771	$< 1.44 \times 10^{-16}$	*uvm2*	⋯
87.1	2398	>21.314	$< 1.38 \times 10^{-17}$	*uvm2*	⋯
3.9	10	>18.852	$< 1.54 \times 10^{-16}$	*uvw2*	⋯
4.1	114	>19.356	$< 9.68 \times 10^{-17}$	*uvw2*	⋯
4.4	10	>18.966	$< 1.39 \times 10^{-16}$	*uvw2*	⋯
25.6	83	>19.614	$< 7.64 \times 10^{-17}$	*uvw2*	⋯
37.3	450	>20.917	$< 2.30 \times 10^{-17}$	*uvw2*	⋯
54.4	450	>20.68	$< 2.86 \times 10^{-17}$	*uvw2*	⋯
73.3	253	>21.153	$< 1.85 \times 10^{-17}$	*uvw2*	⋯
100.5	450	>20.525	$< 3.30 \times 10^{-17}$	*uvw2*	⋯

Note. Columns (1) and (2) give the midtime of the exposure in kiloseconds since the GBM trigger and the length of the exposure divided by 2. Magnitudes are given in the Vega system. Uncertainties are given at the 1σ level. Observations with S/N greater than or equal to 2 were considered detections. For the nondetections, 3σ upper limits are given. The values in this table have not been corrected for Galactic extinction.

Appendix D
MAXI Spectral Analysis and Dust Scattering Mitigation

Source spectra at the first ($T_0 + 2.5$ ks) and second ($T_0 + 8.0$ ks) scans were extracted from a $3.^{\circ}0 \times 4.^{\circ}0$ rectangular region centered on the source (Figure 11, left), corresponding to the FWHM of 1.5° and 1.5°–2° of the PSF for the scan and its perpendicular (anode) directions, respectively (Sugizaki et al. 2011). Since the source was detected near the center of the GSC_4 detector and at the edge of the GSC_5 detector ($\beta = 2^{\circ}$–3°; see Figure 2 in Mihara et al. 2011), we extracted the background spectra from two $2.^{\circ}4 \times 4.^{\circ}0$ rectangular regions before and after scanning the source region, avoiding a shadow region near the center frame of the GSC_4 camera body (at $\beta \simeq 0$) and a high background region in the GSC_5. GSC_4 spectra at or after the scan at 17:04 ($T_0 + 13.6$ ks) were obtained from a circular region within a radius of $1.^{\circ}5$, and the background ones were from an annulus region with the inner and outer radii of $2.^{\circ}0$ and $4.^{\circ}0$ overlapped with a $8.^{\circ}0 \times 3.^{\circ}4$ rectangular region (Figure 11, right). GSC_5 spectra at those scans were not used because of low signal-to-noise data.

We evaluated fluxes of the direct afterglow component in the following two ways: First, we fitted the spectra in the 4–20 keV band where the contribution from the dust scattering component is small (middle rows in Table 7). This led to harder fitted photon indices in the first and second scan spectra, $\Gamma = 1.75 \pm 0.09$, and $\Gamma = 2.07^{+0.28}_{-0.26}$, than those in the simple 2–20 keV fits, the former being closer to that of the first XRT observation, 1.61 ± 0.02.

Next we directly investigated energy spectra of the dust scattering component using the XRT data. To emulate the dust scattering spectrum, we fit the XRT spectra of two bright outer dust-echo rings at $T_0 + 95.4$ ks and $T_0 + 146.7$ ks with the above power-law model with the fixed column densities. The resultant weighted mean power-law spectral index is $\Gamma_{\rm dust} = 3.94 \pm 0.04$. Assuming this value does not change with time, we attempted to fit the GSC spectra at 2–20 keV with a model with two power laws, allowing the normalization of both components and the nondust photon index for the first and second scan spectra to be free (Figure 12). We summarize the fitting results in the lower rows in Table 7. Interestingly, the obtained parameters for the first and second scan spectra are almost perfectly consistent with those in the single power-law fits at 4–20 keV whether the photon index is fixed or not; though the uncertainty of the dust flux (the normalization of the power law with $\Gamma = 3.94$) is large. We also note that the first

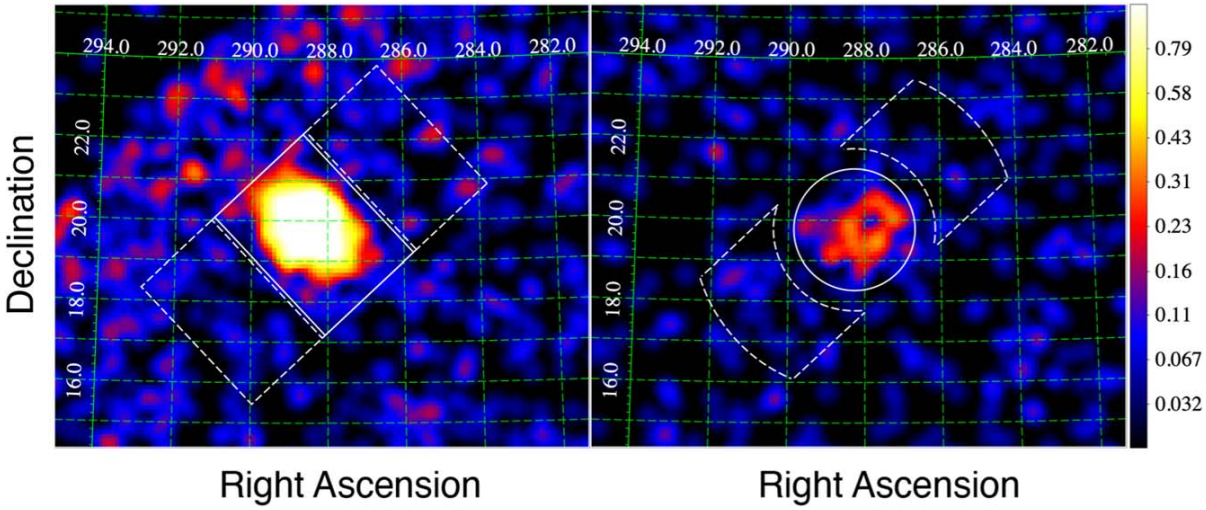

Figure 11. GSC 2–20 keV images obtained with GSC_5 at $T_0 + 2.5$ ks (left) and GSC_4 at $T_0 + 13.6$ ks (right). Source and background regions are shown by the solid lines and the dashed lines, respectively.

Table 7
MAXI Observation Logs and Spectral Fit Results

$T - T_0$ (ks)	Photon Index	Flux (10^{-8} erg cm^{-2} s^{-1}) 0.3–10 keV	Flux (10^{-8} erg cm^{-2} s^{-1}) unabs 0.3–10 keV	Flux (10^{-8} erg cm^{-2} s^{-1}) 4–10 keV	Dust Flux 0.3–10 keV	C-stat/d.o.f.
Single power-law fit (range: 2–20 keV)						
2.459	1.95 ± 0.05	6.98 ± 0.21	$13.54^{+0.85}_{-0.78}$	3.68 ± 0.11	⋯	353/367
	1.85 [f]	6.83 ± 0.19	12.32 ± 0.34	$3.77^{+0.11}_{-0.10}$	⋯	356/368
8.033	$2.22^{+0.16}_{-0.15}$	$1.31^{+0.10}_{-0.09}$	$3.21^{+0.68}_{-0.51}$	0.60 ± 0.05	⋯	180/208
	1.85 [f]	$1.22^{+0.09}_{-0.08}$	2.21 ± 0.15	0.68 ± 0.05	⋯	187/209
13.608	1.85 [f]	0.66 ± 0.08	$1.19^{+0.15}_{-0.14}$	$0.36^{+0.05}_{-0.04}$	⋯	93/84
19.181	1.85 [f]	0.45 ± 0.07	$0.80^{+0.13}_{-0.12}$	0.25 ± 0.04	⋯	59/62
24.757	1.85 [f]	$0.37^{+0.07}_{-0.06}$	$0.66^{+0.12}_{-0.11}$	$0.20^{+0.04}_{-0.03}$	⋯	40/51
30.330	1.85 [f]	0.12 ± 0.06	$0.22^{+0.11}_{-0.10}$	0.07 ± 0.03	⋯	54/37
Single power-law fit (range: 4–20 keV)						
2.459	1.75 ± 0.09	$6.01^{+0.36}_{-0.34}$	$10.10^{+1.18}_{-1.01}$	3.46 ± 0.13	⋯	307/322
	1.85 [f]	6.34 ± 0.23	$11.44^{+0.42}_{-0.41}$	$3.50^{+0.13}_{-0.12}$	⋯	309/323
8.033	$2.07^{+0.28}_{-0.26}$	$1.17^{+0.22}_{-0.18}$	$2.52^{+1.35}_{-0.74}$	0.58 ± 0.06	⋯	145/166
	1.85 [f]	1.05 ± 0.10	$1.90^{+0.19}_{-0.18}$	0.58 ± 0.06	⋯	146/167
13.608	1.85 [f]	0.60 ± 0.12	$1.08^{+0.22}_{-0.21}$	$0.33^{+0.07}_{-0.06}$	⋯	42/36
19.181	1.85 [f]	$0.36^{+0.09}_{-0.08}$	$0.65^{+0.16}_{-0.14}$	$0.20^{+0.05}_{-0.04}$	⋯	43/41
24.757	1.85 [f]	0.30 ± 0.08	$0.55^{+0.15}_{-0.14}$	$0.17^{+0.05}_{-0.04}$	⋯	29/33
30.330	1.85 [f]	$0.13^{+0.09}_{-0.08}$	$0.24^{+0.16}_{-0.15}$	$0.07^{+0.05}_{-0.04}$	⋯	52/32
Two power-law fit						
2.459	1.81 ± 0.12	$6.16^{+0.63}_{-0.57}$	$10.79^{+2.09}_{-1.66}$	$3.47^{+0.20}_{-0.19}$	$1.18^{+0.81}_{-0.87}$	351/366
	1.85 [f]	$6.36^{+0.28}_{-0.27}$	$11.48^{+0.50}_{-0.49}$	3.51 ± 0.15	$0.91^{+0.42}_{-0.41}$	351/367
8.033	$2.14^{+0.16}_{-0.38}$	$1.22^{+0.18}_{-0.33}$	$2.81^{+0.92}_{-1.27}$	$0.59^{+0.07}_{-0.09}$	$0.11^{+0.48}_{-0.11}$	180/207
	1.85 [f]	0.98 ± 0.13	1.77 ± 0.23	0.54 ± 0.07	$0.46^{+0.20}_{-0.19}$	181/208
13.608	1.85 [f]	$0.53^{+0.13}_{-0.12}$	$0.95^{+0.23}_{-0.22}$	0.29 ± 0.07	$0.24^{+0.20}_{-0.18}$	92/83
19.181	1.85 [f]	$0.27^{+0.11}_{-0.10}$	$0.49^{+0.10}_{-0.18}$	$0.15^{+0.06}_{-0.05}$	$0.32^{+0.17}_{-0.16}$	55/61
24.757	1.85 [f]	$0.25^{+0.10}_{-0.09}$	$0.46^{+0.18}_{-0.17}$	0.14 ± 0.05	$0.22^{+0.17}_{-0.15}$	38/50
30.330	1.85 [f]	0.12 ± 0.06	0.22 ± 0.11	$0.07^{+0.03}_{-0.04}$	0.00 ± 0.00	54/36

Note. Flux columns show observed flux at 0.3–10 keV, unabsorbed flux at 0.3–10 keV, and observed flux at 4–10 keV. All the exposure times are 47 s except for 48 s at 21:42:30. All the fluxes are in units of 10^{-8} erg cm^{-2} s^{-1}. The photon index of 1.85 with no error is a fixed value. Note all errors given are 1σ.

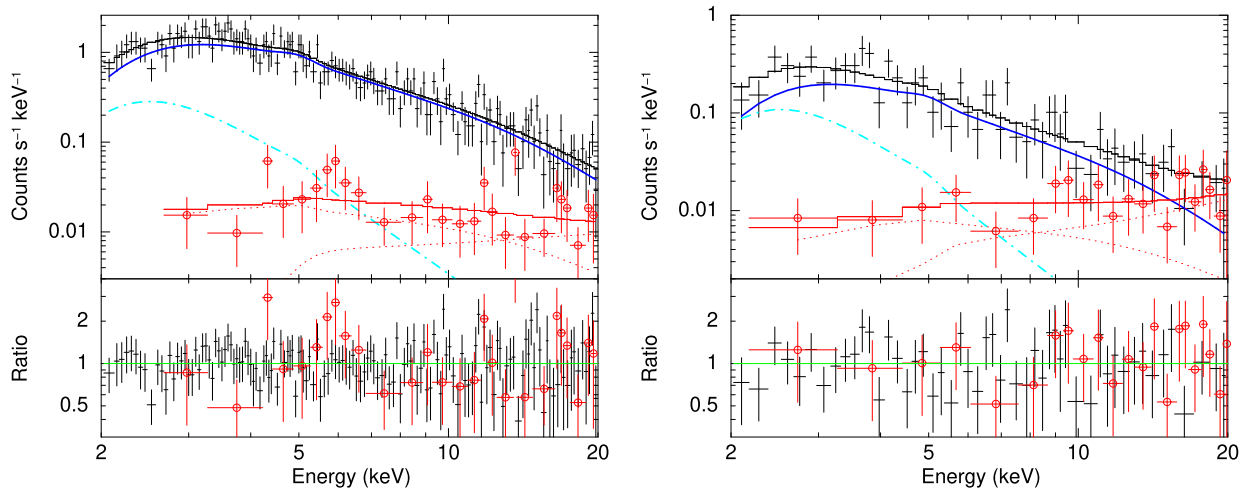

Figure 12. GSC spectra at $T_0 + 2.5$ ks (left panel) and at $T_0 + 8.0$ ks (right). The blue solid lines show the direct power-law component with Γ free for the spectrum at $T_0 + 2.5$ ks and fixed at 1.85 at $T_0 + 8.0$ ks. The light blue dashed lines are the power-law model with $\Gamma = 3.94$. The red points and lines are background data and models, respectively. The background model is the sum of two power laws. The best-fit data to the model ratio is also shown in each panel.

scan spectrum tends to be harder than the second scan one in all the cases.

The differential scattering cross section has energy E and scattering angle θ_s dependence of approximately $\exp(-\alpha E^2\theta_s^2)$ for $\theta_s \ll 1$ where α is a constant of proportional to the square of the size of grain (e.g., Mauche & Gorenstein 1986). Thus, an actual dust scattered component is considered to have a harder spectrum than assumed here especially in the first and second scan observations. If the time and spectral evolution of the dust echo ring is understood, the fitting parameters can be more constrained. This is, however, beyond the scope of this paper. Finally, we note that if we assume $\Gamma = 3.5$ for the scattered power-law component we got a steeper photon index ($\Gamma = 1.75 \pm 0.14$) and a lower 0.3–10 keV absorbed flux of $5.76^{+0.82}_{-0.70} \times 10^{-8}$ erg cm^{-2} s^{-1} for the direct power-law component in the first scan spectrum.

Appendix E
Dust Echo Modeling

In order to examine the properties of the dust scattered echo, images were created from the XRT PC-mode event data over the 0.8–5.0 keV band, where the dust reprocessing cross section peaks. Given the scattered emission evolves radially with time, the images were initially extracted over per snapshot intervals (with typical exposures ranging from 0.3 to 1.6 ks), until the day 22 post trigger when per observation ID (ObsID) images were created (with exposures from 3.3 to 5.2 ks). Vignetting-corrected exposure maps were also generated, spanning the observing times for each image.

Radial profiles were then generated as follows. The GRB position was obtained on a per image basis by fitting the expected XRT PSF model (including a piled-up profile modification when required, as described in Evans et al. 2020) to the imaging data out to 47.″1 where the central source dominates. This position was then used as the location about which radial profiles were generated, initially in 2.″357 linear bins from 0.′79 to 13.′75 radius, following the removal of 12 faint point sources (with count rates less than 3.5×10^{-3} count s^{-1}, determined from 67 ks of late-time data ranging from $T_0 + 43$ to 64 days after the trigger). The central source profile was retained and combined with a nominal background level determined from late-time data to provide the nonhalo background estimate. Example radial profiles are shown in Figure 13, which shows the echo emission expanding and decreasing in intensity with time. Later profiles were stacked to increase signal to noise in the plot, with radial bins scaled so that radial bins correspond to the first profile in the set of stacked observations according to Equation (1) in order to align radial intensity features of different observations.

The plots show clear excess over the PSF from the afterglow emission by the point source, with each peak (i.e., each ring in the image) corresponding to a separate dust cloud along the line of sight.

Approximating the light curve of the prompt emission as a delta function, the radial intensity of the echo, at time $t = t_{\rm GRB} + \Delta t$, plotted in Figure 13 can be written as

$$I_{\rm echo} = \frac{2c \cdot n(D_{\rm Dust})}{\theta^2} \cdot \mathcal{F} \cdot \frac{d\sigma}{d\Omega} \cdot e^{-\tau_{\rm phot}} \qquad \text{(E1)}$$

where $n(D)$ is the dust volume density as a function of distance $D(\theta, \Delta t)$ along the line of sight for a given scattering angle θ and time since the burst Δt, and $\tau_{\rm phot}$ is the optical depth to photoelectric absorption along the line of sight. The observed radial intensity distribution is then given by the convolution of Equation (E1) with the telescope PSF.

The flux of a given cloud of column density N at distance D (used to perform the dist model fits) is given by (Heinz et al. 2016)

$$F = \frac{2\pi cN}{D} \cdot \mathcal{F} \cdot \frac{d\sigma}{d\Omega}. \qquad \text{(E2)}$$

Because the time delay from the prompt emission and the radius θ of each ring are known, Equation (E1) can be used to measure the product of burst fluence, density, and scattering cross section, and, with knowledge of the fluence and a model for the scattering cross section, we can, in principle, solve for the dust density distribution $n_{\rm dust}$ as a function of line-of-sight (LOS) distance and the azimuthal angle along the ring for each observation.

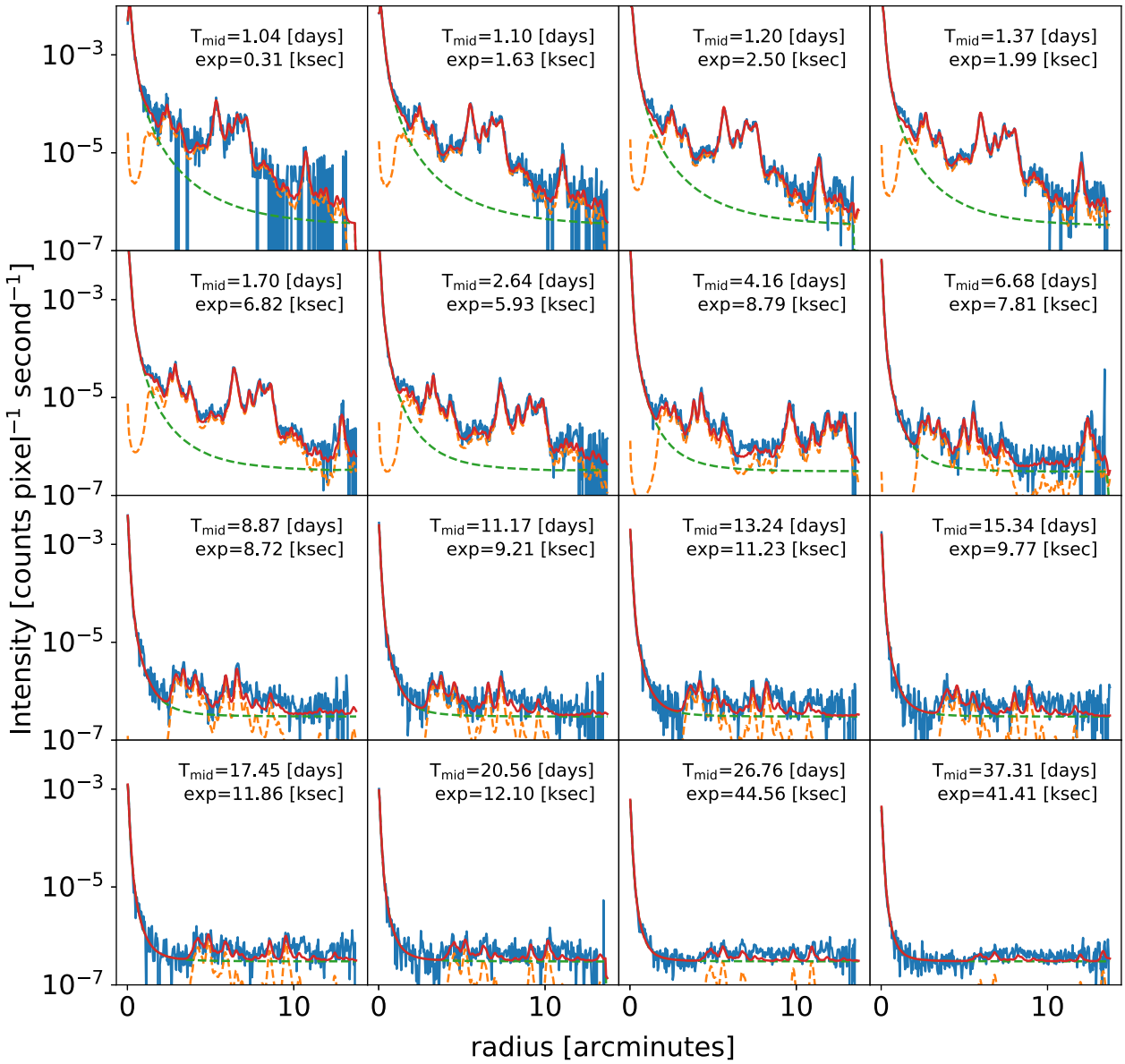

Figure 13. XRT PC-mode radial intensity profiles in the 0.8–5.0 keV band (blue solid lines); later profiles show stacked observations in indicated time windows, with radii scaled to the beginning of the observing window using Equation (1) so that radial intensity features at the same distance appear at the same radius. Overplotted lines show the PSF and background model (green dashed) and the dust model (orange dashed) and the best-fit model (solid red).

In practice, estimating the fluence at soft X-ray energies (where dust scattering is most efficient and where the echo is observed) requires extrapolation from the sensitivity band of the instruments that detected the prompt emission (namely, GBM; S. Lesage et al. 2023, in preparation), corrected for intrinsic absorption. This fluence value, derived using GBM data (after pile-up correction procedures), has an uncertainty of ∼50% that propagates to our results.

In addition, models for the dust scattering cross section vary from cloud to cloud and are themselves not well constrained. Thus, a conservative approach will treat both $d\,\sigma/d\Omega$ and $n_{\rm Dust}$ as functions to be fitted simultaneously, with the understanding that constraints derived for each will carry some degeneracy.

That said, the *relative* column density distribution is well constrained by this process, provided that dust chemistry and grain size distribution do not vary drastically from cloud to cloud.

At typical soft X-ray energies around 2 keV, the scattering cross section is roughly constant at angles smaller than about 100″ while falling off rapidly at larger scattering angles (roughly as $d\,\sigma/d\Omega \propto \theta^{3.5}$). This results in a rapid decline in the intensity and flux of the echo as a function of time as the ring size expands, as can be seen in Figure 13. It further implies that, beyond a ring radius of about 100″, smaller rings, which are farther away, will have a larger intensity per column density compared to larger rings, which are closer to the observer.

On the other hand, the Galactic latitude of GRB 221009A of $b = 4.^{\circ}3$ suggests that the Galactic column density distribution should be dominated by nearby dust within the plane, within a few kiloparsecs. For example, the dust at the intersection of the

LOS with the Solar circle on the far side of the Galaxy would lie 780 pc (almost 8 dust scale heights, e.g., Li et al. 2018) above the Galactic plane, where we would not expect to see substantial amounts of dust (however, any dust present at those distances will benefit from the intensity enhancement discussed in the previous paragraph).

To constrain the dust column density and cross section models, we decomposed the dust distribution along the line of sight into 100 logarithmically spaced bins and determined the least squares fit for the column density for each bin. To this end, we constructed 1D XRT PSFs to approximate the radial profile for each dust ring. We then defined the fitting function as given by Equation (E1) for each column density component. We added the point-source PSFs for each profile to the fitting function. We then fitted all 100 components simultaneously to all the background-subtracted and radial intensity profiles between days 1 and 42 post-burst. The resulting inferred density distribution is plotted in Figure 4.

Appendix F
Broadband SED Construction

The BAT survey spectra are produced using the `BatAnalysis` Python package (T. Parsotan et al. 2023, in preparation). Using the HEASoft `batsurvey` script, the `BatAnalysis` package calculates the count rate of the GRB in each of the 8 energy bins used in the BAT survey (14–20, 20–24, 24–35, 35–50, 50–75, 75–100, 100–150, and 150–195 keV) and the errors associated with each energy bin. The package also generates the detector response matrix using the HEASoft `batdrmgen` script for the BAT survey observation of interest.

For the time intervals of the two SEDs, we created time-sliced X-ray spectra being careful to limit dust echo contamination (see Section 3.2). The source spectral files were grouped to $\geqslant$20 counts per energy bin. The spectral files were normalized to correspond to the 0.3–10 keV flux of the afterglow at $T_0 + 4.2$ ks or $T_0 + 43$ ks. The flux used to normalize a given spectrum is determined by fitting a power law to the data within the SED time range, and the best-fit decay index is used to compute the flux at the mid-point of the SED, in the same way as was done for the UVOT data.

To build the optical spectral files, we follow the methodology provided in Schady et al. (2010). This essentially sets the count rates in the spectral files to that determined at an instantaneous epoch by extrapolating the UVOT light curves. In order to obtain the count rates at the instantaneous epoch, we first combined the data from the different filters into a single-flow light-curve filter. The light curves of the different filters were normalized to that in the v filter. The normalization was determined by fitting a power law to each of the light curves in a given time range simultaneously. The power-law indices were constrained to be the same for all the filters, and the normalizations were allowed to vary between the filters. The ratios of the power-law normalizations between each filter and the v filter were then used to shift the individual light curves to the same normalization as the v filter, thus resulting in a single filter light curve. To construct the two SEDs at $T_0 + 4.2$ ks and $T_0 + 43$ ks, we first determine the temporal slope from the single filter light curve within the corresponding time interval. By fixing the power-law index at this value, we then fit a power law to the individual filter light curves. We use the derived normalizations to compute the count rate and count-rate error at the required time, which was then applied to the relevant spectral file.

Appendix G
BAT Trigger Simulation

To estimate the intrinsic rate of such events, we utilize the BAT trigger simulator (Lien et al. 2014) to calculate the detectability of the prompt emission at different redshifts under different representative instrumental setups. Specifically, our setup uses (1) one standard average background level, (2) four different locations on the BAT image plane (i.e., Grid IDs of [14, 15, 16, 17] or equivalent boresight angles of [56°, 45°, 27°, 0°]), which represent different detector sensitivity and cover different locations within the BAT field of view, and (3) four different numbers of enabled detectors (29,000, 22,000, 18,000, and 15,000; these numbers represent the change of average number of enabled detectors from 2005 to 2022). We ran simulations with a combination of each of these setups with a sample of redshifts from $z = 0.1$, to $z = 12$, with increments of $\Delta z = 1.0$ (i.e., $z = 0.1$, 1.0, 2.0,...,12.0). The simulation results are summarized in Table 8.

For each setup, we estimate the expected number of detections based on the highest detectable redshift $z_{\rm lim}$ and an assumed intrinsic rate with the following equation:

$$N_{{\rm det},i_{\rm setup}} = R_{\rm GRB}(z < z_{\rm lim})\, f_{\rm survey}\, f_{\rm fov}\, f_{\rm grid}\, f_{\rm ndet}\,. \tag{G1}$$

$R_{\rm GRB}(z < z_{\rm lim})$ is the all-sky intrinsic rate up to the redshift limit for this burst to be detected by BAT with a specific setup of Grid ID and number of enabled detectors, and is calculated by integrating the comoving rate by taking into account of the volume of the universe through the following equation (see, e.g., Lien et al. 2011, for details of the derivation):

$$R_{\rm GRB}(z < z_{\rm lim}) = 4\pi \int_0^{z_{\rm limit}} R_{\rm GRB,comov}(z=0) \times \frac{r_{\rm comov}^2}{(1+z)} \frac{dr_{\rm comov}}{dz}\, dz, \tag{G2}$$

where the comoving distance $r_{\rm comov}(z) = (\frac{C}{H_0}) \int_0^z 1/H(z)\, dz$. $f_{\rm survey}$ is the fraction of time that BAT is capable of triggering, and we adopt $f_{\rm survey} = 0.8$ based on the study in Lien et al. (2016). $f_{\rm fov} = (2.1\ {\rm sr})/(4\pi\ {\rm sr})$ is the fraction of sky covered by the entire BAT field of view down to a partial coding fraction of $\sim$0.1, and $f_{\rm grid} = [0.460, 0.346, 0.109, 0.085]$ is the fraction of BAT field of view for Grid IDs (14), (15), (16), and (17).[46] In other words, $f_{\rm fov} \times f_{\rm grid}$ is the fraction of bursts in the entire sky that would have the partial coding fraction of the specific Grid ID. $f_{\rm ndet}$ is the fraction of GRBs in the BAT field of view that would occur with this number of enabled detectors. For simplicity, we assume an equal number of GRBs occur with these four numbers of enabled detectors. That is, $f_{\rm ndet} = 0.25$.

The total number of detections can then be calculated by adding up $N_{{\rm det},i_{\rm setup}}$ for all 16 combinations of instrumental

[46] https://asd.gsfc.nasa.gov/Craig.Markwardt/bat-cal/solid-angle/

Table 8
Detectable Redshift Limit for Each Instrumental Setup

Grid ID	ndet	$z_{\rm lim}$
17	29000	11
17	22000	11
17	18000	11
17	15000	11
16	29000	11
16	22000	11
16	18000	11
16	15000	11
15	29000	11
15	22000	10
15	18000	9
15	15000	9
14	29000	5
14	22000	4
14	18000	4
14	15000	3

Note. "Grid ID" indicates the location at the BAT image plane and corresponds to different partial coding fractions and thus different detector sensitivities. "ndet" refers to the number of enabled detectors.

setups listed in Table 8. That is,

$$N_{\rm det,tot} = \sum_{i_{\rm setup}=1}^{16} N_{{\rm det},i_{\rm setup}}. \quad \text{(G3)}$$

We assume a flat intrinsic comoving rate of $R_{\rm GRB,comov}(z=0)$ and adjust the value until the detection rate matches with that of a GRB 221009A–like event. We set the upper limit of the BAT detection rate of such events to be 1 per 18 yr of the Swift mission lifetime, because the prompt emission of the burst actually occurred outside of the BAT field of view. This gives us a corresponding upper limit of $R_{\rm GRB,comov}(z=0) \leqslant 6.1\times10^{-4}\,{\rm Gpc^{-3}\,yr^{-1}}$. Integrating this flat comoving rate from $z=0$, to $z=12$, we obtain an upper limit on the all-sky rate of GRB 221009A–like events to be $0.5\,{\rm yr^{-1}}$. Comparing to the all-sky intrinsic long-GRB rate of $\sim4571\,{\rm yr^{-1}}$ in Lien et al. (2014), the fraction of GRB 221009A–like events is roughly $0.5/4571 \leqslant 1.0\times10^{-4}$.

ORCID iDs

Maia A. Williams https://orcid.org/0000-0002-0025-3601
Jamie A. Kennea https://orcid.org/0000-0002-6745-4790
S. Dichiara https://orcid.org/0000-0001-6849-1270
Wataru B. Iwakiri https://orcid.org/0000-0002-0207-9010
Andrew P. Beardmore https://orcid.org/0000-0001-5186-5950
P. A. Evans https://orcid.org/0000-0002-8465-3353
Sebastian Heinz https://orcid.org/0000-0002-8433-8652
Amy Lien https://orcid.org/0000-0002-7851-9756
S. R. Oates https://orcid.org/0000-0001-9309-7873
Hitoshi Negoro https://orcid.org/0000-0003-0939-1178
S. Bradley Cenko https://orcid.org/0000-0003-1673-970X
Douglas J. K. Buisson https://orcid.org/0000-0002-5341-6929
Dieter H. Hartmann https://orcid.org/0000-0002-8028-0991
Gaurava K. Jaisawal https://orcid.org/0000-0002-6789-2723
N. P. M. Kuin https://orcid.org/0000-0003-4650-4186
Stephen Lesage https://orcid.org/0000-0001-8058-9684
Kim L. Page https://orcid.org/0000-0001-5624-2613
Tyler Parsotan https://orcid.org/0000-0002-4299-2517
Dheeraj R. Pasham https://orcid.org/0000-0003-1386-7861
B. Sbarufatti https://orcid.org/0000-0001-6620-8347
Michael H. Siegel https://orcid.org/0000-0003-1817-3009
George Younes https://orcid.org/0000-0002-7991-028X
Elena Ambrosi https://orcid.org/0000-0002-9731-8300
M. G. Bernardini https://orcid.org/0000-0001-6106-3046
S. Campana https://orcid.org/0000-0001-6278-1576
Milvia Capalbi https://orcid.org/0000-0002-9558-2394
Regina Caputo https://orcid.org/0000-0002-9280-836X
Antonino D'Aì https://orcid.org/0000-0002-5042-1036
P. D'Avanzo https://orcid.org/0000-0001-7164-1508
V. D'Elia https://orcid.org/0000-0002-7320-5862
Massimiliano De Pasquale https://orcid.org/0000-0002-4036-7419
R. A. J. Eyles-Ferris https://orcid.org/0000-0002-8775-2365
Elizabeth Ferrara https://orcid.org/0000-0001-7828-7708
Keith C. Gendreau https://orcid.org/0000-0001-7115-2819
Jeffrey D. Gropp https://orcid.org/0000-0002-9090-5553
Nobuyuki Kawai https://orcid.org/0000-0001-9656-0261
Noel Klingler https://orcid.org/0000-0002-7465-0941
Sibasish Laha https://orcid.org/0000-0002-2002-6350
A. Melandri https://orcid.org/0000-0002-2810-2143
Tatehiro Mihara https://orcid.org/0000-0002-6337-7943
Michael Moss https://orcid.org/0000-0002-1103-7082
Paul O'Brien https://orcid.org/0000-0002-5218-1899
Julian P. Osborne https://orcid.org/0000-0002-1041-7542
David M. Palmer https://orcid.org/0000-0001-7128-0802
Matteo Perri https://orcid.org/0000-0003-3613-4409
E. Sonbas https://orcid.org/0000-0002-6909-192X
Michael Stamatikos https://orcid.org/0000-0001-7253-8553
Rhaana Starling https://orcid.org/0000-0001-5803-2038
G. Tagliaferri https://orcid.org/0000-0003-0121-0723
Aaron Tohuvavohu https://orcid.org/0000-0002-2810-8764
Silvia Zane https://orcid.org/0000-0001-5326-880X
Houri Ziaeepour https://orcid.org/0000-0001-8164-3582

References

Arnaud, K. A. 1996, in ASP Conf. Ser. 101, Astronomical Data Analysis Software and Systems V, ed. G. H. Jacoby & J. Barnes (San Francisco, CA: ASP), 17
Astropy Collaboration, Robitaille, T. P., Tollerud, E. J., et al. 2013, A&A, 558, A33
Barthelmy, S. D., Barbier, L. M., Cummings, J. R., et al. 2005, SSRv, 120, 143
Beardmore, A. P., Willingale, R., Kuulkers, E., et al. 2016, MNRAS, 462, 1847
Bloom, J. S., Frail, D. A., & Sari, R. 2001, AJ, 121, 2879
Bloom, J. S., Perley, D. A., Li, W., et al. 2009, ApJ, 691, 723
Breeveld, A. A., Landsman, W., Holland, S. T., et al. 2011, in AIP Conf. Ser. 1358, ed. J. E. McEnery, J. L. Racusin, & N. Gehrels (Melville, NY: AIP), 373
Brethauer, D., Grefenstette, B., Racusin, J., et al. 2022, GCN, 32695, 1
Brown, P. J., Roming, P. W. A., Milne, P., et al. 2010, ApJ, 721, 1608
Burrows, D. N., Hill, J. E., Nousek, J. A., et al. 2005, SSRv, 120, 165
Campana, S., Mangano, V., Blustin, A. J., et al. 2006, Natur, 442, 1008
Cash, W. 1979, ApJ, 228, 939
Castro-Tirado, A. J., Sanchez-Ramirez, R., Hu, Y. D., et al. 2022, GCN, 32686, 1
Cenko, S. B., Frail, D. A., Harrison, F. A., et al. 2011, ApJ, 732, 29
D'Avanzo, P., Ferro, M., Brivio, R., et al. 2022, GCN, 32755, 1
De Pasquale, M., Evans, P., Oates, S., et al. 2009, MNRAS, 392, 153
de Ugarte Postigo, A., Izzo, L., Pugliese, G., et al. 2022, GCN, 32648, 1
Dichiara, S., Gropp, J. D., Kennea, J. A., et al. 2022, GCN, 32632, 1
Evans, P. A., Beardmore, A. P., Page, K. L., et al. 2007, A&A, 469, 379
Evans, P. A., Beardmore, A. P., Page, K. L., et al. 2009, MNRAS, 397, 1177
Evans, P. A., Page, K. L., Beardmore, A. P., et al. 2023, MNRAS, 518, 174

Evans, P. A., Page, K. L., Osborne, J. P., et al. 2020, ApJS, 247, 54
Foreman-Mackey, D., Farr, W., Sinha, M., et al. 2019, JOSS, 4, 1864
Frail, D. A., Kulkarni, S. R., Sari, R., et al. 2001, ApJL, 562, L55
Galama, T. J., Vreeswijk, P. M., van Paradijs, J., et al. 1998, Natur, 395, 670
Gehrels, N., Chincarini, G., Giommi, P., et al. 2004, ApJ, 611, 1005
Gendreau, K. C., Arzoumanian, Z., & Okajima, T. 2012, Proc. SPIE, 8443, 844313
Ghisellini, G., Ghirlanda, G., Nava, L., & Firmani, C. 2007, ApJL, 658, L75
Guha, A., & Nicholson, P. 2022, GCN, 32745, 1
Heinz, S., Burton, M., Braiding, C., et al. 2015, ApJ, 806, 265
Heinz, S., Corrales, L., Smith, R., et al. 2016, ApJ, 825, 15
Huang, Y., Hu, S., Chen, S., et al. 2022, GCN, 32677, 1
Iwakiri, W., Jaisawal, G. K., Younes, G., et al. 2022, GCN, 32694, 1
Izzo, L., Saccardi, A., Fynbo, J. P. U., et al. 2022, GCN, 32765, 1
Kann, D. A., Agayeva, S., Aivazyan, V., et al. 2023, arXiv:2302.06225
Kann, D. A., & Agui Fernandez, J. F. 2022, GCN, 32762, 1
Kennea, J. A., Williams, M. & Swift Team 2022, GCN, 32635, 1
Kobayashi, K., Negoro, H., Nakajima, M., et al. 2022, GCN, 32756, 1
Kuin, N. P. M., Dichiara, S. & Swift/UVOT Team 2022, GCN, 32656, 1
Kulkarni, S. R., Frail, D. A., Wieringa, M. H., et al. 1998, Natur, 395, 663
Laha, S., Wadiasingh, Z., Parsotan, T., et al. 2022, ApJ, 929, 173
Laskar, T., Alexander, K. D., Margutti, R., et al. 2023, arXiv:2302.04388
Levan, A. J., Lamb, G. P., Schneider, B., et al. 2023, arXiv:2302.07761
Li, L., Shen, S., Hou, J., et al. 2018, ApJ, 858, 75
Lien, A., Chakraborty, N., Fields, B. D., & Kemball, A. 2011, ApJ, 740, 23
Lien, A., Sakamoto, T., Barthelmy, S. D., et al. 2016, ApJ, 829, 7
Lien, A., Sakamoto, T., Gehrels, N., et al. 2014, ApJ, 783, 24
Liu, Y.-Q., Modjaz, M., Bianco, F. B., & Graur, O. 2016, ApJ, 827, 90
Margutti, R., Milisavljevic, D., Soderberg, A. M., et al. 2014, ApJ, 797, 107
Maselli, A., Melandri, A., Nava, L., et al. 2014, Sci, 343, 48
Mathis, J. S., Rumpl, W., & Nordsieck, K. H. 1977, ApJ, 217, 425
Matsuoka, M., Kawasaki, K., Ueno, S., et al. 2009, PASJ, 61, 999
Mauche, C. W., & Gorenstein, P. 1986, ApJ, 302, 371
Meegan, C., Lichti, G., Bhat, P. N., et al. 2009, ApJ, 702, 791
Mihara, T., Nakajima, M., Sugizaki, M., et al. 2011, PASJ, 63, S623
Morgan, A. N., Perley, D. A., Cenko, S. B., et al. 2014, MNRAS, 440, 1810
Nasa High Energy Astrophysics Science Archive Research Center (Heasarc) 2014, HEAsoft: Unified Release of FTOOLS and XANADU, Astrophysics Source Code Library, ascl:1408.004
Negoro, H., Kohama, M., Serino, M., et al. 2016, PASJ, 68, S1
Negoro, H., Nakajima, M., Kobayashi, K., et al. 2022, ATel, 15651, 1
Negro, M., Di Lalla, N., Omodei, N., et al. 2023, arXiv:2301.01798
Nousek, J. A., Kouveliotou, C., Grupe, D., et al. 2006, ApJ, 642, 389
Oates, S. R., Page, M. J., Schady, P., et al. 2009, MNRAS, 395, 490
O'Connor, B., Troja, E., Ryan, G., et al. 2023, arXiv:2302.07906
Perley, D. A., Cenko, S. B., Corsi, A., et al. 2014, ApJ, 781, 37
Piran, T. 2004, RvMP, 76, 1143
Planck Collaboration, Aghanim, N., Akrami, Y., et al. 2020, A&A, 641, A6
Poole, T. S., Breeveld, A. A., Page, M. J., et al. 2008, MNRAS, 383, 627
Racusin, J. L., Liang, E. W., Burrows, D. N., et al. 2009, ApJ, 698, 43
Remillard, R. A., Loewenstein, M., Steiner, J. F., et al. 2022, AJ, 163, 130
Roming, P. W. A., Kennedy, T. E., Mason, K. O., et al. 2005, SSRv, 120, 95
Sari, R., Piran, T., & Halpern, J. P. 1999, ApJL, 519, L17
Sari, R., Piran, T., & Narayan, R. 1998, ApJL, 497, L17
Schady, P., Mason, K. O., Page, M. J., et al. 2007, MNRAS, 377, 273
Schady, P., Page, M. J., Oates, S. R., et al. 2010, MNRAS, 401, 2773
Schlafly, E. F., & Finkbeiner, D. P. 2011, ApJ, 737, 103
Schnoor, P. W., Nicholson, P., & Welch, D. L. 2022, GCN, 32744, 1
Siegel, M. H., Porterfield, B. L., Linevsky, J. S., et al. 2014, AJ, 148, 131
Sugizaki, M., Mihara, T., Serino, M., et al. 2011, PASJ, 63, S635
Tiengo, A., Pintore, F., Mereghetti, S., & Salvaterra, R. 2022, ATel, 15661, 1
Vasilopoulos, G., Karavola, D., Stathopoulos, S. I., & Petropoulou, M. 2023, MNRAS, Advance Access
Vasilopoulos, G., & Petropoulou, M. 2016, MNRAS, 455, 4426
Veres, P., Burns, E., Bissaldi, E., et al. 2022, GCN, 32636, 1
Willingale, R., Starling, R. L. C., Beardmore, A. P., Tanvir, N. R., & O'Brien, P. T. 2013, MNRAS, 431, 394
Yamazaki, R., Sato, Y., Sakamoto, T., & Serino, M. 2020, MNRAS, 494, 5259
Zhang, B., Fan, Y. Z., Dyks, J., et al. 2006, ApJ, 642, 354